

JWST imaging of the Pleiades: Anisotropy of turbulence in the cold neutral medium

G. Vigoureux¹, N. Flagey², F. Boulanger¹, A. Noriega-Crespo², V. Guillet³, A. J. Alvarez-Castro⁴, N. deJesus-Rivera⁴, E. Ally¹, J. M. Delouis⁵, E. Falgarone¹, B. Godard¹, P. Guillard⁶, F. Levrier¹, P. Lesaffre¹, A. Marcowith³, M. A. Miville-Deschénes¹, and G. Pineau des Forêts^{7,8}

¹ Laboratoire de Physique de l'ENS, Université PSL, CNRS, F-75005 Paris

² Space Telescope Science Institute, 3700 San Martin Drive, Baltimore, MD 21218

³ Laboratoire Univers et Particules, Université de Montpellier, F-34095 Montpellier

⁴ Universidad de Puerto Rico, Rio Piedras, San Juan, PR 00931

⁵ Laboratoire d'Océanographie Physique et Spatiale, Univ. Brest, CNRS, Ifremer, IRD, F-29200 Brest

⁶ Sorbonne Université, CNRS, UMR 7095, Institut d'Astrophysique de Paris, F-75014 Paris

⁷ Université Paris-Saclay, CNRS, Institut d'Astrophysique Spatiale, F-91405, Orsay

⁸ Observatoire de Paris, Université PSL, Sorbonne Université, LUX, F-75014 Paris

Received: August 27, 2025 ; Accepted: January 26, 2026

ABSTRACT

Interstellar medium studies rely on magnetohydrodynamic turbulence as a framework for interpretation. In this context, the statistical characterization of interstellar observations is of prime importance. We present a new perspective on diffuse interstellar matter by analyzing *James Webb* Space Telescope (JWST) observations of the Pleiades nebula with NIRCam. These observations are remarkable in that they provide a "microscope" view of the cold neutral medium (CNM) with a spatial resolution of 0.2 mpc (40 au). A 2D Fourier analysis was used to characterize the structure of polycyclic aromatic hydrocarbon (PAH) emission in regions near and far from the Pleiades star Merope. To produce maps of the interstellar emission, stars and galaxies were filtered out. The final step in the data cleaning involved subtracting a component, in Fourier space, which we inferred to be a residual of the near-infrared cosmic background. The PAH emission power spectra are highly anisotropic. PAH emission power spectra are highly anisotropic at all scales, with a constant level of power anisotropy. The magnetic field orientation, as derived from the *Planck* dust polarization data, aligns with the PAH anisotropy. The spectra are well fitted with a break-free power law, suggesting that we do not observe a specific scale for energy dissipation. Power-law indices are -3.5 near Merope and -3 in the more distant field. These findings are discussed in relation to interstellar turbulence that may be driven by the Pleiades stars. The JWST observations of the Pleiades offer a new viewpoint for comparing observations and theoretical models, as they examine physical scales at which turbulence in the CNM is subsonic and decoupled from the thermal instability. The observations may indicate that the turbulent energy cascade in the CNM is anisotropic.

Key words. ISM, Magnetic fields, Turbulence

1. Introduction

Studies of the cold interstellar medium (ISM) frequently rely on numerical simulations of magnetohydrodynamic (MHD) turbulence as a theoretical model (Hennebelle & Falgarone 2012; Burkhardt 2021). In this context, the statistical analysis of interstellar observations is crucial to interpreting observations (Richard et al. 2025). This paper presents a new perspective, using observations of the Pleiades nebula by the *James Webb* Space Telescope (JWST) with the Near-Infrared Camera (NIRCam).

The Pleiades reflection nebula is an iconic astronomical object familiar to a wide audience and also a prime scientific target for studies of the dusty ISM (Gibson & Nordsieck 2003a,b; Gibson 2007). We are observing a chance encounter between a star cluster and diffuse molecular gas (Gordon & Arny 1984; Herbig & Simon 2001; Ritchey et al. 2006). The brightest members of the Pleiades cluster are late-B stars at a distance of 135 pc (Abramson 2018) illuminating their surrounding ISM over a few parsecs (Gibson & Nordsieck 2003a). The stellar illumination enables the ISM structure to be observed at smaller angular

scales than is usually possible. The reflection nebulosity offers a spectacular view of the filamentary structure of the diffuse ISM.

Many studies have relied on dust continuum observations to determine the power spectrum of interstellar matter (Gautier et al. 1992; Ingalls et al. 2004; Miville-Deschénes et al. 2007, 2010, 2016). The advent of *Planck* made it possible to extend this type of analysis to polarized dust emission (Planck Collaboration 2020a), which established the statistical alignment of diffuse interstellar structures with the magnetic field direction on parsec scales (Clark et al. 2015; Planck Collaboration 2016c). This result has been interpreted as a hallmark of magnetized interstellar turbulence (Caldwell et al. 2017; Kandel et al. 2017). In a broader context, the JWST offers a unique opportunity. Its angular resolution and sensitivity to the emission of polycyclic aromatic hydrocarbons (PAHs) enable imaging of the cold ISM at finer scales than was previously possible. At the distance of the Pleiades, the angular resolution of NIRCam corresponds to a spatial scale of 0.2 mpc, at which we may be able to identify signatures of dissipation of turbulence, in particular through ion-neutral friction (Burkhart et al. 2015; Hu et al. 2024). Although there is observational evidence of structure in the cold neutral

medium (CNM) at these scales, existing observations are too sparse to conduct a statistical study (Heiles 1997; Stanimirović & Zweibel 2018).

The purpose of this work is to demonstrate and capitalize on the potential of JWST for diffuse ISM studies. We used PAH emission to investigate the structure of the cold magnetized ISM. In fact, PAHs are tightly coupled to the gas through collisions (Omont 1986) and to magnetic field lines. In the physical conditions of the Pleiades nebula – specifically the gas density and temperature and the radiation field strength – PAHs exist partly as cations and partly in neutral form (Flagey et al. 2006). However, both charged and neutral PAHs are coupled to magnetic field lines because their charge state varies on timescales much shorter than their drag time through collisions with the gas (Lepp & Dalgarno 1988).

The paper is organized as follows. Section 2 introduces the JWST observations and outlines the data processing steps to generate images of diffuse emission. Our 2D Fourier analysis of these images is described in Sects. 3 and 4. In Sect. 5 we discuss the results of the data analysis in relation to interstellar turbulence. Finally, Sect. 6 summarizes our main results. The paper includes three appendices. Appendix A details and illustrates the methods used to remove stars and mask galaxies from the JWST images. Appendix B provides a broader context for the JWST observations, in which we characterize the magnetized interstellar matter associated with the Pleiades nebula using *Planck* data. In Appendix C we use the observations to characterize the physical conditions and demonstrate that the JWST observations of the Pleiades probe the structure of the CNM.

2. Imaging the diffuse emission from PAHs

This section introduces the JWST observations (Sect. 2.1) and outlines the data processing steps that were performed to derive maps of diffuse emission from PAHs (Sect. 2.2).

2.1. JWST observations

The NIRCam instrument (Rieke et al. 2023) was used to image two fields, each measuring 6' by 2.2' as part of the GO 2143 program. Field 1 is centered approximately 2' to the east of the bright Pleiades star Merope (23 Tau), and Field 2 about 10' to the southeast of Merope. The top images in Fig. 1 show the location of the two fields within the Pleiades. The two images at the bottom were produced by the JWST pipeline. For this paper, we used version 1.18.0 of the calibration software.

The two fields were imaged in the F212N filter, centered on the 1-0 S(1) H₂ line, and the F335M filter that includes the 3.3–3.4 μ m emission bands from PAHs. We also obtained observations at both sky positions in the F200W and F277W filters. The observations in the short- and long wavelength channels are executed simultaneously, in the spectral filters F212N with F335M and F200W with F277W. For each pointing, the integration time was 10⁴ s for the H₂ and PAH observations, and 4000 s for the wide filters. In this study, we only analyzed the F335M data. The data obtained using the three additional filters will be presented in a future paper.

The long channel of NIRCam comprises two square detectors, each with 2000 pixels square and a field of view of 129''. We used the FULLBOX 6TIGHT¹ dithering pattern to obtain multiple offset pointings of the camera and cover the rectangular

field without gaps. The dithering also mitigates bad pixels and flat-field uncertainties; it significantly reduces the data noise on the smallest angular scales, where brightness variations are the smallest. We did not use secondary sub-pixel dithers because the fine sampling of the point-spread function (PSF) is not essential to our observations.

2.2. Maps of diffuse emission

In order to study the PAH emission, we needed to separate the diffuse emission in the F335M filter image from numerous point sources (mostly stars) and compact sources (mostly galaxies). We did this in four main steps, which we outline here. More details are given in Appendix A.

- We modeled and subtracted the large diffraction spikes from two bright stars, Merope and PQ Tau. These two stars are outside the JWST fields, but their spikes are prominent structures in Field 1. One of the Merope spikes is also visible in Field 2.
- We subtracted from a first approximation the diffuse emission using a multi-scale median filter. This step yields background-subtracted images, which we then used to identify and remove point sources and compact sources located within the JWST fields.
- We subtracted point sources using an empirical template of the JWST PSF. This template was obtained by stacking background-subtracted images centered on point sources to sub-pixel accuracy. Point sources are subtracted by fitting the PSF template over small images centered on each source. We did not use the core of the point sources in this fit because it is often saturated.
- Compact extended sources — including galaxies and the saturated cores of bright stars — are identified on maps after background, spike, and point source subtraction, and are then masked. The sky area we masked is set by a brightness threshold applied to maps in which spikes, multi-scale background, and point sources have been subtracted (see Appendix A). The masked areas are filled in with the multi-scale background maps.

To assess systematic uncertainties associated with the data cleaning, we checked how sensitive the results of our data analysis are to the brightness threshold used to create the mask. For the fiducial mask, 9% of the sky pixels are masked. We used two alternative masks, the light mask (for which this fraction is 5%) and the heavy mask (14%).

For statistical analysis, we divided the dither pointings into two sets $h1$ and $h2$, which we used to produce a pair of images for each of the two fields. The two images in each pair cover the same sky region, but have independent statistical noise. Each of the four images (2 pairs) is processed separately by following steps (1) to (4). Separate background maps and masks are computed for each image. After step (4), the difference between the two images in each pair allows us to identify and mask a small number of glitches present in one of the two images. Mathematically, for each field, we obtained two independent maps of diffuse emission, d_{h1} and d_{h2} , from sky images s_{h1} and s_{h2} with spikes and stars subtracted:

$$\begin{aligned} d_{h1} &= M_{h1} s_{h1} + (1 - M_{h1}) b_{h1} \\ d_{h2} &= M_{h2} s_{h2} + (1 - M_{h2}) b_{h2}, \end{aligned} \quad (1)$$

where M_{h1} and M_{h2} denote masks and b_{h1} and b_{h2} the background maps.

¹ NIRCam page at <https://jwst-docs.stsci.edu/jwst-near-infrared-camera/nircam-observing-modes/>

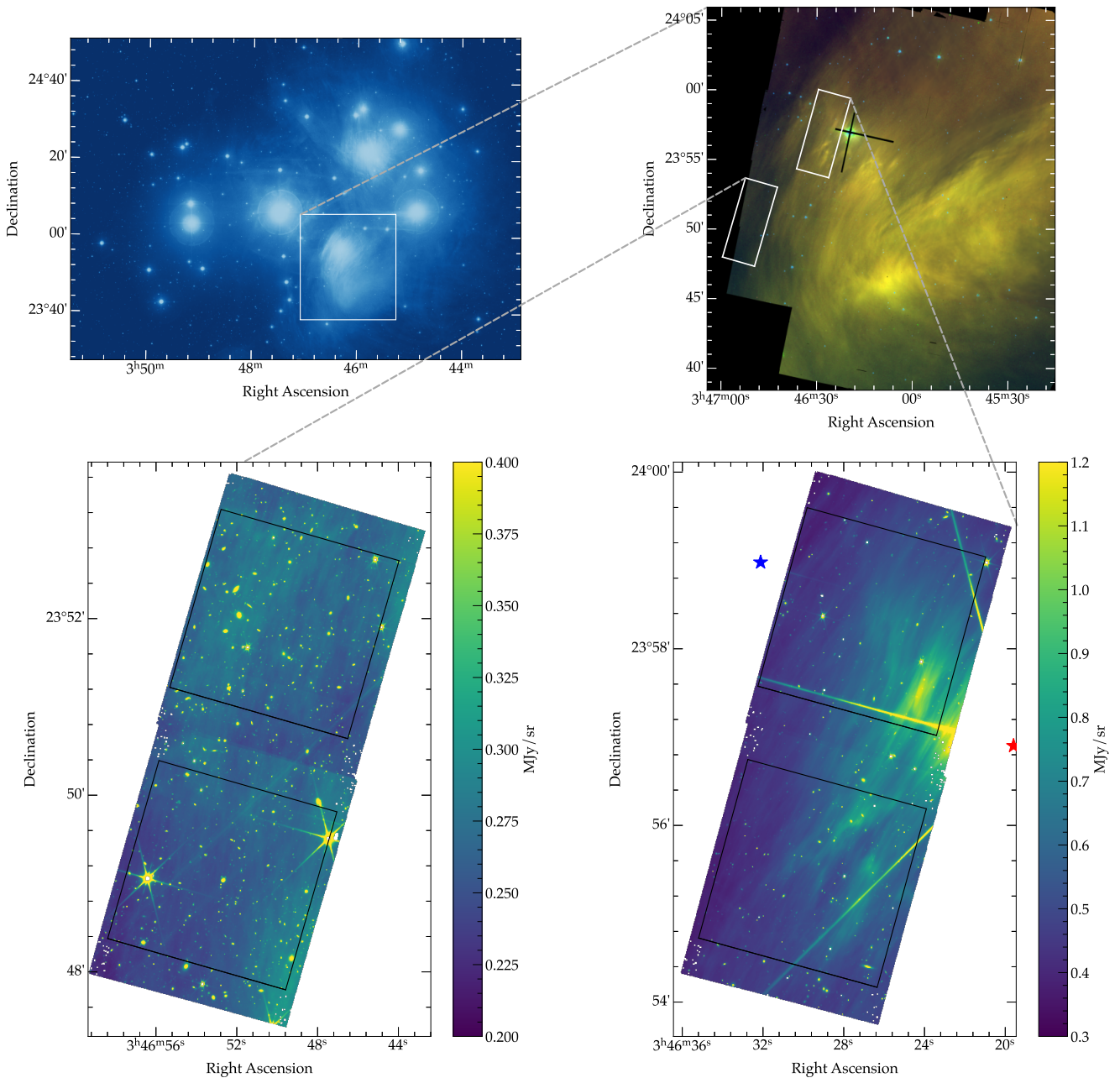


Fig. 1. Overview of the F335M observations in the Pleiades. Top left: Cutout from the digitized Palomar Sky Survey (POSS II; $\lambda_{eff} \sim 480$ nm). Top right: Three-color composition from *Spitzer*/IRAC (red: $8.0 \mu\text{m}$, green $5.8 \mu\text{m}$, blue $3.6 \mu\text{m}$). Merope saturates the IRAC detectors and causes the dark cross. Bottom: F335M observations at both positions in our JWST/NIRCam program. Field 2 is on the left and Field 1 on the right. Note that the color scale is not the same in the two images. The footprint of the *Spitzer*/IRAC image is shown in the POSS II image, and those of the JWST/NIRCam images are shown in the *Spitzer*/IRAC image as rectangles. The red and blue stars on the rightmost JWST image indicate the positions of Merope and PQ Tau. The four black square boxes display the location of the square maps analyzed in this paper. The Cut 1 images are north of the Cut 2 images.

For power spectrum analysis, we cut out two square images, with 2000 pixels on each side, in each field. The positions of these cuts are drawn with solid black lines in the JWST images displayed in Fig. 1. The center positions and orientation of these images can be found in Table 1. We analyzed eight square images (four pairs) from which diffraction spikes, stars, galaxies, and glitches have been removed. The maps of diffuse emission in each of the four pairs are presented in Fig. 2. The four images show a similar pattern with nearly parallel striations. The JWST/NIRCam pixel size $\text{pix}_{\text{JWST}} = 0.063''$ corresponds to $4.1 \cdot 10^{-2}$ mpc (8.5 au) at the distance of the Pleiades. The full size

of each square image is 80 mpc. Compared with other observational means, one can say that the JWST offers us a "microscope" view at the diffuse ISM.

Pairs of square images are used to compute cross-power spectra unbiased by data noise. To emphasize and demonstrate the importance of data cleaning, we calculated the cross-power spectra at each stage for Field 1 Cut 1 as an example. The results of this analysis are shown in Fig. 3. The top spectrum represents the unprocessed JWST image that features spikes, stars, and galaxies. In contrast, the bottom spectrum corresponds to the final image of the diffuse emission. The intermediate curves in

dicate the cross-power spectra of the maps of spikes, stars, and galaxies that were subtracted from the original data. Data cleaning leads to a decrease in the amplitude of the spectra by up to 4 orders of magnitude for the highest k .

The mean brightness has been subtracted from the JWST images because it is a model value (Rigby et al. 2023) introduced in the data pipeline that does not separate interstellar emission from the zodiacal, stellar, and extragalactic backgrounds. To estimate the mean PAH emission, we measured the mean brightness averaged over each image field of view at $12\mu\text{m}$, using the Wide-Field Infrared Explorer (WISE) data (Wright et al. 2010). The values listed in Table 1 represent the emission from the Pleiades nebula with the large-scale Galactic contribution, measured off the nebula, subtracted out. The brightness ratios between the diffuse Galactic emission in the F335M NIRCam filter and the WISE $12\mu\text{m}$ filter, $I_{3.5}/I_{12}$ values listed in Table 1, were measured by correlating the structure of the $12\mu\text{m}$ emission with the multi-scale background F335M maps. These values are consistent with dust emission models (Compiègne et al. 2011; Draine & Li 2007) and observations².

3. Fourier analysis

This section presents the Fourier analysis of the images of diffuse emission shown in Fig. 2.

3.1. Computation and statistical uncertainties

We computed the 2D cross-power spectrum, $P_{2D}(k, \theta)$, for the pair of square images d_{h1} and d_{h2} introduced in Eq. 1:

$$P_{2D}(k, \theta) = \Re \left(\widehat{M_A d_{h1}} \times \widehat{M_A d_{h2}}^* \right), \quad (2)$$

where the wavenumber k and the angle θ , measured from the celestial north modulo π , are polar coordinates in the Fourier plane. \Re denotes the real part, the hat symbol the Fourier transform, and the asterisk the complex conjugate. M_A represents the image apodization applied to avoid edge effects in the Fourier transform³.

We use $P_b^{d_1 \times d_2}(k, \theta)$ to denote the mean value of $P_{2D}(k, \theta)$, within bins of width Δk and $\Delta\theta$, and $P_b(k)$ the cross-power spectrum averaged over angles. To estimate uncertainties on $P_b^{d_1 \times d_2}(k, \theta)$ and $P_b(k)$, we used the following formulae:

$$\sigma (P_b^{d_1 \times d_2})^2 = (2(P_b^{d_1 \times d_2})^2 + 2P_b^{d_1 \times d_2} \times N + N^2) / n_b \quad (3)$$

$$n_b = \frac{4\pi}{A_{\text{map}}} \Delta\theta k \Delta k, \quad (4)$$

where N is the noise power spectrum of images d_{h1} and d_{h2} , n_b is the number of Fourier modes in the bin b , and A_{map} is the effective area of the sky covered by the maps after apodization. We refer to Knox (1995) and Hivon et al. (2002) for a mathematical derivation and the numerical assessment of these formulae, and to Viero et al. (2013) and Córdova Rosado et al. (2024) for their application to the analysis of infrared sky maps. To apply this formula, we required the noise power spectra N for each pair of square maps. These were estimated from the power spectrum of

² The color ratio $I_{3.5}/I_{12}$ is related to the size distribution of PAHs. The diffuse ISM values, derived from the analysis of the DIRBE and *Spitzer*/IRAC data, are in the range 2 to $6 \cdot 10^{-2}$ (Dwek et al. 1997; Flagey et al. 2006)

³ We used the Tukey function in the SciPy python package with its default parameters.

the difference $d_{h1} - d_{h2}$, for Fields 1 and 2 separately. The factor 2 arising from the difference was taken into account.

The left term in Eq. 3 represents the cosmic variance, the minimum uncertainty on the sky spectrum estimate for noise-free data, the right term is the variance of the data noise, and the middle term the random correlation between sky emission and data noise. The left term dominates for the lowest wavenumbers, where the maps comprise a small number of independent modes, and the right term dominates for the highest wavenumbers, where the signal-to-noise ratio on the sky emission is the lowest.

Figure 4 shows the cross-power spectra $P_b(k)$ of the four JWST images. Hereafter, the wavenumber expressed in units of $\text{pix}_{\text{JWST}}^{-1}$ in the bottom axis is converted into physical scales in au on the top axis for a distance to the Pleiades of 135 pc (Melis et al. 2014; Abramson 2018). The spectra are corrected for the signal attenuation by the telescope beam, using the power spectrum of the PSF image produced with the STPSF Python package for our NIRCam observations in the F335M filter. The PSF varies across the field of the camera, but this effect is ignored because it is smeared out by the raster mapping of the sky. The spectra in Fig. 4 all show a flattening at high k . This is not due to data noise, because the noise is not correlated between maps d_{h1} and d_{h2} .

3.2. Anisotropy model

To analyze the anisotropy of the diffuse emission, we averaged $P_{2D}(k, \theta)$ into logarithmic bins of k with $\Delta k/k = 0.2$ and linear bins of θ , modulo π , with $\Delta\theta = 4^\circ$, which do not overlap. We use k_i and θ_j to denote the bin centers and $P_{i,j}$ the binned value of P_{2D} . The uncertainty on $P_{i,j}$ is estimated using Eq. 3. We modeled the angular dependence of $\log P_{i,j}$ with a Gaussian profile. Mathematically our data model is as follows:

$$\log (P_{i,j}) = \Gamma_i \exp \left(-\frac{(\theta_j - \theta_0)^2}{2\sigma_\theta^2} \right) + B_i. \quad (5)$$

The angle θ_0 defines the orientation, perpendicular to the striations seen in the images, for which the power is maximum, and σ_θ measures the dispersion of this orientation over the images. Γ_i represents the ratio of maximum to minimum power while B_i the minimum power within the k_i bin. We performed a global fit of $\log(P_{i,j})$ with values of θ_0 and σ_θ independent of k . These two model parameters are listed in Table 2 for each of the four images in Fig. 2. The values of θ_0 match the dust polarization angles measured at the image centers using *Planck* polarization data at 353 GHz (see Appendix B and Fig. B.2). In emission, the dust polarization angle is perpendicular to the projection of the magnetic field on the plane of the sky. As θ_0 measures the orientation perpendicular to the striations, we conclude that the filamentary structure of the PAH emission is aligned with the magnetic field projection. This is similar to what is observed on parsec scales with *Planck* data (Clark et al. 2015; Planck Collaboration 2016c).

Figure 5 presents the angular profiles of the power spectrum amplitude obtained for Cut 1 in Field 1. The profiles are shown for five k -bins, equally spaced in $\log(k)$ from large to small angular scales from top to bottom; the dashed lines represent the model fit to the data. We note that the profile appears to be less anisotropic for high wavenumbers⁴.

⁴ The fit shown in Fig. 5 allows for small variations of θ_0 and σ_θ between the five k bins.

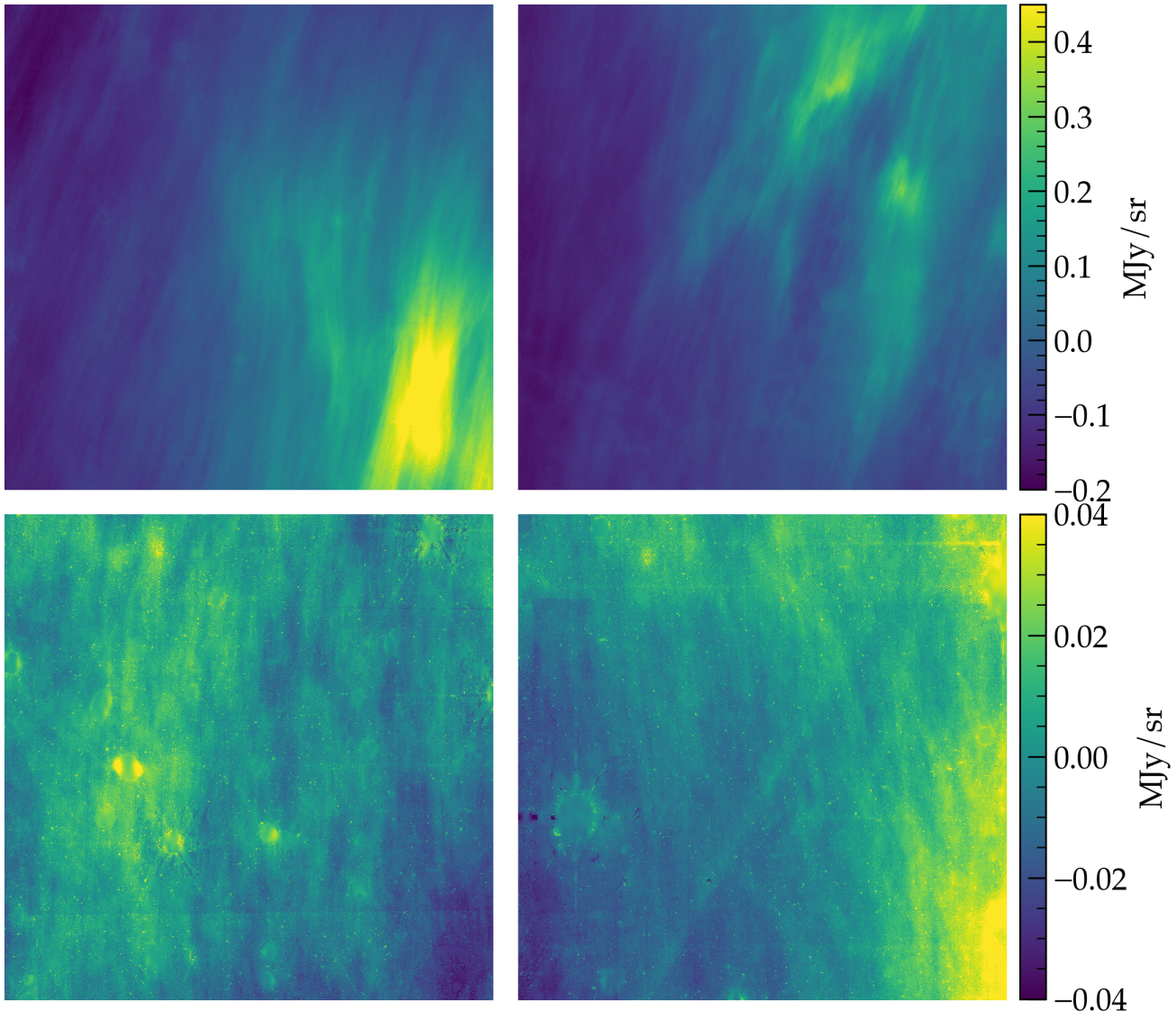


Fig. 2. JWST images of diffuse sky emission. The panels show the average image of the four pairs we analyzed; the top row shows Field 1 images, and the bottom row Field 2 images. The Cut 1 images are to the left and the Cut 2 images to the right. The mean values of each image are set to zero. The center positions and the position angles of the vertical axes of the images can be found in Table 1.

The model allowed us to derive the power spectra for the orientations parallel and perpendicular to the striations in the sky image:

$$\begin{aligned} P_{i,\parallel} &\equiv 10^{B_i} / P_{\text{PSF}} \\ P_{i,\perp} &\equiv 10^{(\Gamma_i + B_i)} / P_{\text{PSF}}, \end{aligned} \quad (6)$$

where P_{PSF} is the power spectrum of the JWST PSF. The division by P_{PSF} corrects the spectra for the attenuation of the beam. The data error bars are propagated to P_{\parallel} and P_{\perp} by the fitting procedure. Our definition of P_{\parallel} corresponds to the power spectrum of the emission parallel to the mean orientation of the striations⁵. As Cho & Vishniac (2000) pointed out in their analysis of MHD turbulence simulations, the Fourier transformation only partially measures the 3D anisotropy of the PAH emission because the striations orientation varies across the sky and along

the line of sight. The angular widths of the profiles in Fig. 5 reflect the dispersion of the orientation of the striations across the image. These widths are significant. They exceed the dispersion of the polarization angles (12°) reported by Planck Collaboration (2016a) in their analysis of *Planck* data in the southern Galactic cap.

3.3. Cosmic near-infrared background residual

Figures 4 and 5 indicate that the power spectra include an isotropic emission component, which prevails at high k values. We characterized this component, which we identified as an extragalactic residual left after data cleaning.

The isotropic component is most readily apparent in the P_{\parallel} spectra of Field 2 Cuts 1 and 2 displayed in Fig. 6, because in these spectra the PAH contribution is the smallest. One can clearly see that the two spectra flatten toward high k . Figure 6 shows fits of the P_{\parallel} spectra with a model including two power laws: a steep one representing the PAH contribution and a shal-

⁵ This is true provided that the Gaussian in Eq. 5 is negligible at 90° of θ_0 , a condition that is satisfied for the values of σ_{θ} in Table 2.

Table 1. JWST cutout images.

Image	RA J2000 (a)	Dec J2000 (a)	PA deg (b)	I_{12} MJy sr $^{-1}$ (c)	$10^2 \times I_{3.5}/I_{12}$ (d)
Field1			-15.4		
Cut 1	3:46:26.61	23:58:18.5		7.0 ± 0.2	11.6 ± 0.7
Cut 2	3:46:29.55	23:55:27.4		8.5 ± 0.2	6.1 ± 1.0
Field2			-16.1		
Cut 1	3:46:49.64	23:51:56.3		3.7 ± 0.2	4.4 ± 1.8
Cut 2	3:46:52.72	23:49:5.7		3.3 ± 0.2	3.5 ± 0.9

Notes. (a) Coordinates of image centers. (b) Position angle of the long axis of the JWST mosaic with respect to the north direction measured positive toward the east (counterclockwise direction). (c) Mean emission at $12 \mu\text{m}$ averaged over each of the Pleiades images, measured using the WISE full resolution image. The background contribution is subtracted. (d) Emission ratio derived from a linear correlation of the NIRCam F335M background image and the WISE data.

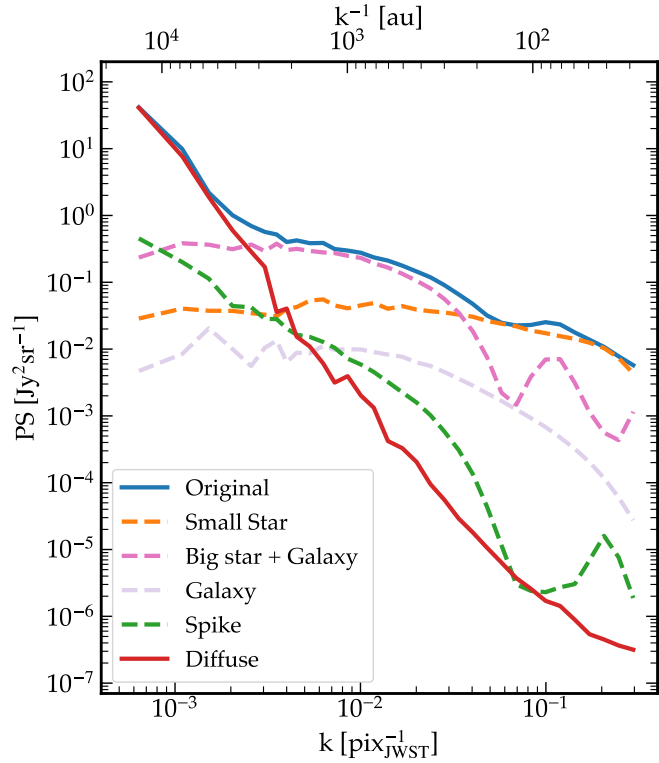


Fig. 3. Power spectra of Field 1 Cut 1 at different steps of the data cleaning. The top spectrum is that of the initial JWST image with the stars, their spikes, and galaxies. The bottom is that of the image at the end of cleaning. The dashed lines show the spectra of the maps of stars, spikes, and galaxies subtracted from the JWST image. The wavenumber is expressed in units of $\text{pix}_{\text{JWST}}^{-1}$ on the bottom axis and au on the top axis.

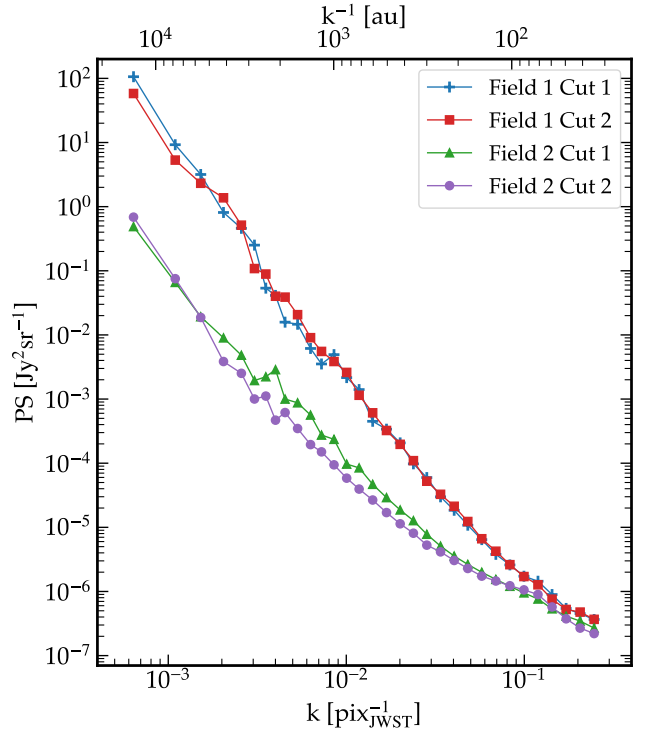


Fig. 4. Cross-power spectra for the four JWST images. Distinct colors and symbols identify the spectra of the images listed in the top-right corner. The spectra are corrected for beam attenuation. Due to the large dynamic range of the four spectra, the statistical error bars are too small to be visible on the plot.

low one representing the isotropic component. For the isotropic component, the same power law is used for Cuts 1 and 2. We performed the data fit for the fiducial, light and heavy masks. The amplitudes and spectral indices of the isotropic component are listed in Table 3. The amplitude and spectral index of the isotropic component are consistent for the fiducial and heavy masks. The reduced χ^2 of the fit is good for the fiducial mask but poor for the light and heavy masks. For the light mask, the isotropic component is dominant for all k and the fit does not succeed in separating the PAH and the isotropic components. For the heavy mask, the amplitude of the isotropic component differs significantly between Cuts 1 and 2.

The spectral index of the isotropic component, about -1.2 , coincides with the value measured for the clustering of faint extragalactic sources combined into a diffuse extragalactic background. The cosmic near-infrared background (CIB) was detected with Infrared Array Camera (IRAC) *Spitzer* data. The measurements reported by Kashlinsky et al. (2012) for the IRAC $3.5 \mu\text{m}$ channel can be directly compared with the results of our JWST analysis. The spectral index of the isotropic component is consistent with the *Spitzer* CIB power spectra, and the amplitude is one order of magnitude smaller. We conclude that the isotropic

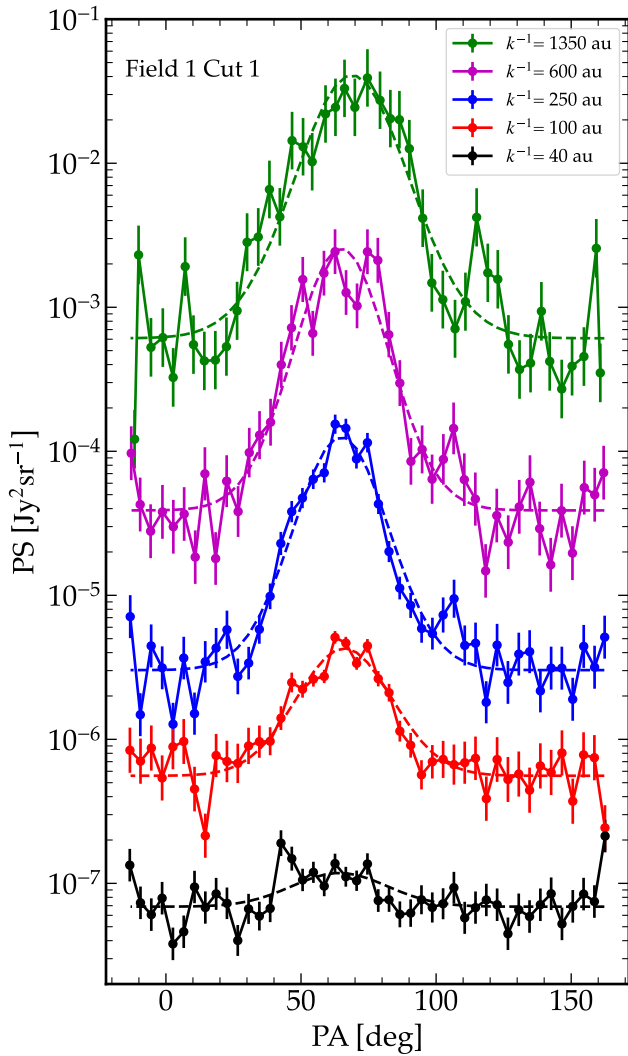


Fig. 5. Angular dependence of the power spectrum amplitude for the Field 1 image Cut 1. The angular dependence is plotted for the 5 k values listed in the top-right corner. The position angle (horizontal axis) is measured modulo π with respect to the celestial north and positive to the east. The dashed lines show the fits of the Gaussian model in Eq. 5 to the profiles.

component is a residual CIB, which remains after the masking of extragalactic sources⁶.

4. Power spectra of PAH emission

In this section we derive power spectra of the Pleiades PAH emission using JWST data. To obtain these spectra, we needed to subtract the CIB residual. This was achieved through three distinct methods, each based on different hypotheses. In Sect. 4.1 we assume that the CIB residual is the same in our two fields, both close to and far from Merope, and we used the latter for subtraction. In Sect. 4.2 we use the anisotropy of the Pleiades emission to subtract the isotropic CIB residual. Section 4.3 presents fits of the Field 1 spectra using two power laws to represent the PAH contribution and the CIB residual.

⁶ We note that the spectra in Fig. 6 do not exhibit flattening at high k , which could be interpreted as shot noise from faint sources at the JWST detection limit.

Table 2. Parameters of the anisotropy fit and dust polarization angles.

Field	θ_0 deg. (a)	σ_θ deg. (a)	ψ deg. (b)
Field 1			
Cut 1	64.9 ± 0.2	17.7 ± 0.2	57 ± 11
Cut 2	58.6 ± 0.2	15.4 ± 0.2	62 ± 7
Field 2			
Cut 1	72.6 ± 0.6	20.2 ± 0.8	77 ± 9
Cut 2	81.6 ± 0.8	20.8 ± 1.3	86 ± 5

Notes. (a) Parameters characterizing the angle dependence of P_{2D} in Eq. 5. (b) Dust polarization angle at the position of the image centers measured using *Planck* polarization data at 353 GHz (see Appendix B).

Table 3. Power-law fits of the residual spectrum.

Mask	A_{res} [Jy 2 sr $^{-1}$] (a)	α_{res} (b)	χ^2 (c)
Fiducial	$1.4 \pm 0.1 10^{-5}$	-1.23 ± 0.025	2.8
Light	$5.9 \pm 0.8 10^{-5}$	-1.40 ± 0.056	24
Heavy	$1.2 \pm 0.2 10^{-5}$	-1.24 ± 0.060	13

Notes. (a): Amplitude of the power law at wavenumber $k_0 = 10^{-2} \text{ pix}_{\text{JWST}}^{-1}$. (b): Spectral index of the power law. (c): Reduced χ^2 of the fit.

Table 4. Power-law fits of the difference between the spectra of Field 1 and Field 2.

Image	$10^3 A_d$ [Jy 2 sr $^{-1}$] (a)	α_d (b)	Mask (c)	$I_{3.5}$ [MJy sr $^{-1}$] (d)
Cut 1	1.93 ± 0.14	-3.47 ± 0.07	F	0.26
	1.95 ± 0.14	-3.43 ± 0.07	L	
	1.91 ± 0.15	-3.66 ± 0.07	H	
Cut 2	2.06 ± 0.09	-3.52 ± 0.04	F	0.25
	2.09 ± 0.11	-3.53 ± 0.05	L	
	2.03 ± 0.10	-3.65 ± 0.05	H	

Notes. (a): Amplitude of the power law at wavenumber $k_0 = 10^{-2} \text{ pix}_{\text{JWST}}^{-1}$. (b): Spectral index of the power law. (c): Mask used to clean the data. F, L and H stand for fiducial, light and heavy masks (see Sect. 2.2). (d): Median brightness at $3.5 \mu\text{m}$ of diffuse emission computed on the Field 1 - Field 2 difference maps.

4.1. Power spectra from the spatial difference

For each spectrum $P_b(k)$ obtained for Cuts 1 and 2 of Field 1, we subtracted the mean of the Field 2 power spectra for Cuts 1 and 2. The difference subtracts the CIB residual and a potential contribution from the Galactic background to the PAH spectra. This approach does not make use of the anisotropy fit, which restricts the range of k bins that can be measured with relevant accuracy. The differences in spectra are presented in Fig. 7. The dashed lines represent power-law fits:

$$\Delta P_b(k)/P_{\text{PSF}}(k) = A_d \left(\frac{k}{k_0} \right)^{\alpha_d}, \quad (7)$$

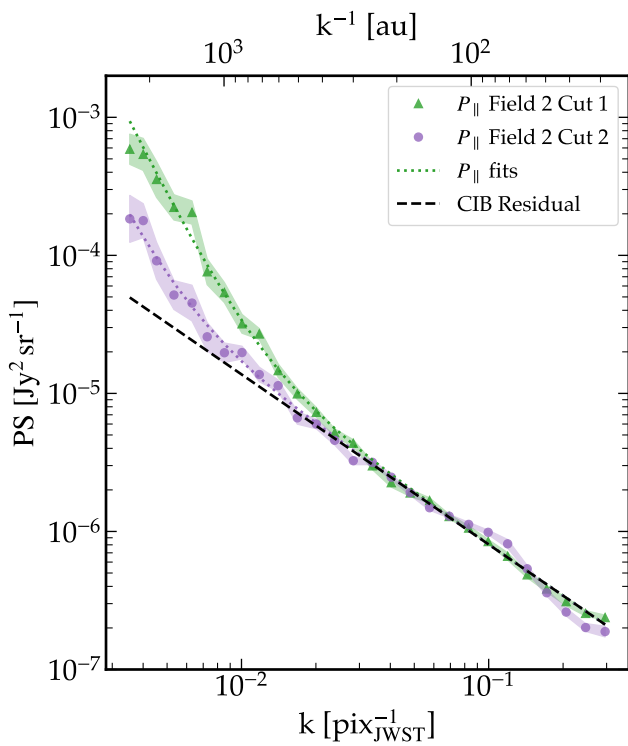


Fig. 6. Power spectra for the parallel orientation of Field 2 Cuts 1 and 2. The color shadings indicate 1σ uncertainties. The dashed black line shows the power-law fit of the component that we interpret as a CIB residual. The dotted lines show the data fit using the sum of two power laws to account for the PAH and residual components.

Table 5. Power-law fits of spectra from the anisotropy difference.

Field	A_a Jy 2 sr $^{-1}$	α_a	Mask
	(a)	(b)	
Field 1			
Cut 1	$1.3 \pm 0.1 10^{-2}$	-3.54 ± 0.05	F
	$1.3 \pm 0.1 10^{-2}$	-3.53 ± 0.05	L
	$1.3 \pm 0.1 10^{-2}$	-3.63 ± 0.06	H
Cut 2	$1.3 \pm 0.1 10^{-2}$	-3.49 ± 0.04	F
	$1.2 \pm 0.1 10^{-2}$	-3.44 ± 0.04	L
	$1.3 \pm 0.1 10^{-2}$	-3.56 ± 0.05	H
Field 2			
Cut 1	$3.5 \pm 0.3 10^{-4}$	-3.05 ± 0.06	F
	$2.6 \pm 0.3 10^{-4}$	-2.82 ± 0.08	L
	$3.8 \pm 0.4 10^{-4}$	-3.15 ± 0.06	H
Cut 2	$1.4 \pm 0.1 10^{-4}$	-2.94 ± 0.06	F
	$1.4 \pm 0.1 10^{-4}$	-2.80 ± 0.06	L
	$1.4 \pm 0.1 10^{-4}$	-2.94 ± 0.06	H

Notes. (a): Parameters of the power-law fit to $P_{\perp} - P_{\parallel}$ for $k_0 = 10^{-2} \text{ pix}_{\text{JWST}}^{-1}$ in Eq. 8. (b): Masks used to compute power spectra. F, L and H stand for fiducial, light and heavy.

where the division by P_{PSF} corrects for the signal attenuation by the JWST beam.

The fit parameters, the amplitude A_d and the spectral index α_d , are listed in Table 4. The table also includes the mean \bar{I} of the sky emission measured after source masking and OFF subtraction. Figure 7 shows the spectra, and Table 4 lists the fit results, for the three masks. The light and heavy masks are used to assess

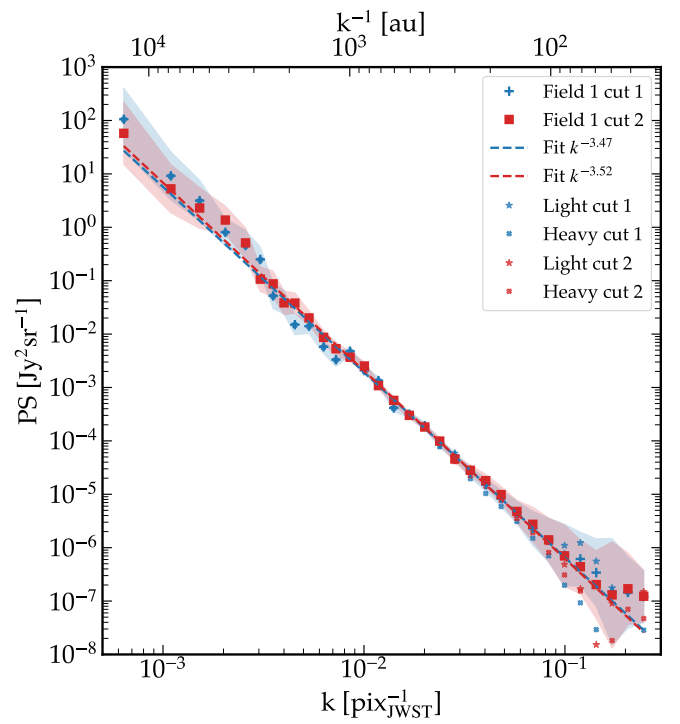


Fig. 7. Power spectra computed for JWST Field 1 images Cuts 1 and 2. The color shadings display 1σ uncertainties. The dashed lines show the power-law fits. The spectra obtained with the light and heavy masks are plotted with smaller symbols: circles and stars.

systematic uncertainties. The data points in Fig. 7 show a noticeable steepening of the spectra at high k for the heavy mask. The difference in the spectral index is slightly larger than the statistical error. This may be due to the lack of small-scale structure in the multi-scale background used to fill in the masked areas.

In this work, we assumed that on the spatial scales probed by the Pleiades JWST data, PAH emission traces the gas column density. For scales smaller than the line-of-sight depth of the emitting medium, the spectral index of the column density power spectrum is identical to that of the 3D density field (Cho & Lazarian 2003; Brunt et al. 2010). We therefore proceed under the assumption that the PAH power spectrum is a proxy for the gas density power spectrum.

The spectral index that we measure matches the reference spectral index for MHD turbulence (Iroshnikov 1964; Kraichnan 1965). It is also consistent with the index inferred by Armstrong et al. (1995) for electron density fluctuations in the local ISM by analyzing pulsar scintillation measurements on scales below 0.3 mpc.

To compare with previous measurements of dust power spectra of the diffuse ISM, we refer to the spectra measured by Gibson (2007) in the Pleiades and by Miville-Deschénes et al. (2016) for an independent field at high Galactic latitude. These spectra, which were obtained by analyzing images of dust scattered light, are the closest observational match to our analysis in terms of angular resolution. For far-infrared dust emission, we also consider results derived from *Herschel* observations by Miville-Deschénes et al. (2010) and Auclair et al. (2024) with angular resolutions of 30 and 15'', respectively. The spectra reported in these four dust studies with spectral indices ranging from -2.7 to -2.95 are shallower than the two shown in Fig. 7.

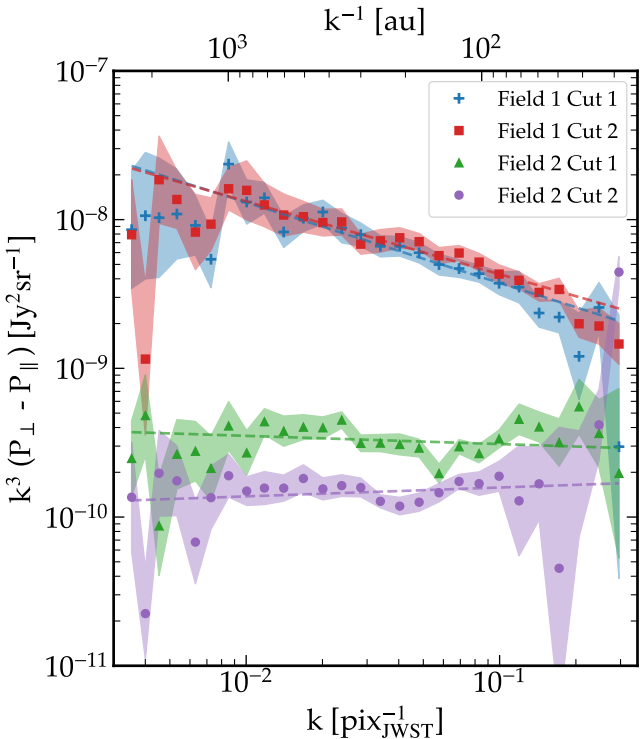


Fig. 8. Difference between the power spectra P_{\perp} and P_{\parallel} for the four JWST images. The difference is scaled by k^3 to reduce the dynamic range. The 1σ uncertainties are represented with shaded colors. The dashed lines represent least square fits to the spectra's differences.

4.2. Power spectra from anisotropy

In our second approach, we assume that the residual CIB is isotropic and obtain power spectra for each of the JWST images by taking the difference $P_{\perp} - P_{\parallel}$. These differences are shown in Fig. 8. To highlight the difference in slope between the Field 1 and 2 images, the spectra are scaled by k^3 . The dashed lines represent power-law fits to the spectra:

$$P_{\perp} - P_{\parallel} = A_a \left(\frac{k}{k_0} \right)^{\alpha_a}, \quad (8)$$

The fit parameters A_a and α_a for each of the images are listed in Table 5. We also list values for the light and heavy masks to assess systematic errors. The differences with the values for the fiducial mask are minor. It is satisfying to obtain values for the power-law indices of the spectra, which are consistent with those obtained for the Field 1 cuts using the spatial difference (see Table 4).

4.3. Two-component fit

We present a third approach where we fit the P_{\perp} and P_{\parallel} spectra separately. In this fit, we assume that the CIB residual is isotropic and well approximated by a power law. The equations of the data model are as follows:

$$\begin{aligned} P_{\parallel} &= A_{0,\parallel} (k/k_0)^{\alpha_{\parallel}} + A_R (k/k_0)^{\alpha_R} \\ P_{\perp} &= A_{0,\perp} (k/k_0)^{\alpha_{\perp}} + A_R (k/k_0)^{\alpha_R}, \end{aligned} \quad (9)$$

where the PAH power spectra are fitted with power laws that have distinct amplitudes and spectral indices.

We performed a Monte Carlo Markov chain (MCMC) analysis to sample the joint posterior distribution of the model parameters. We utilized the EMCEE python package as described

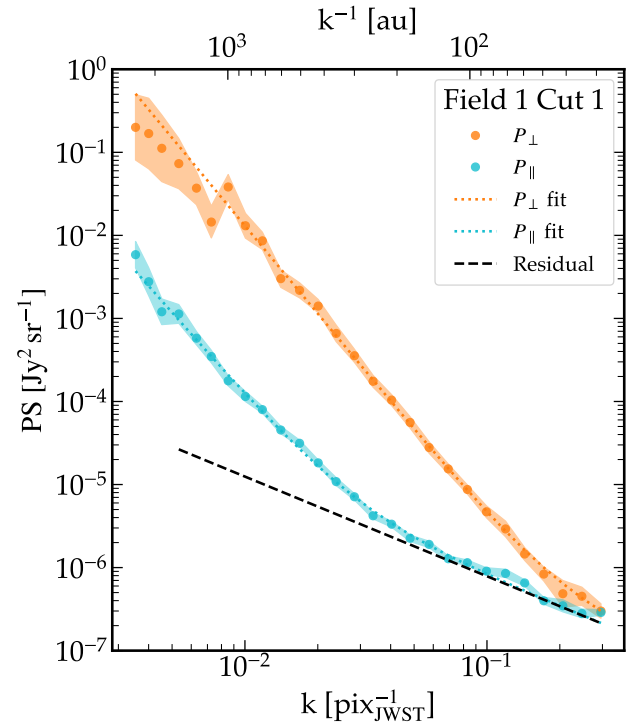


Fig. 9. Fit with two power laws of P_{\perp} and P_{\parallel} for the Field 1 image Cut 1. The dotted orange and cyan lines represent the data fits of P_{\perp} and P_{\parallel} , respectively, while the dashed black line represents the power-law fit of the CIB residual. The shaded areas around the data points indicate the 1σ error bars of the spectra.

by Foreman-Mackey et al. (2013) in accordance with their recommendations. We used a Gaussian likelihood. The priors force the three amplitudes $A_{0,\perp}$, $A_{0,\parallel}$, and A_R to be positive, and the spectral indices α_{\perp} and α_{\parallel} to be negative. In addition, we set a Gaussian prior in the spectral index $\alpha_R = -1.2$ with a dispersion of 0.2 (1σ). This prior follows from the fit of P_{\parallel} for Field 2 images illustrated in Fig. 6. As this prior makes use of Field 2 data, we ran the MCMC analysis only for the two Field 1 images.

The model parameters with their error bars are listed in Table 6. The table lists the median values of the posterior distribution and error bars computed from the 16 and 84 percentiles. As shown in Fig. 9 for Field 1 Cut 1, the model provides a good fit for both P_{\parallel} and P_{\perp} . The amplitude A_R of the CIB residual is consistent with that measured for parallel spectra of Field 2, within error bars (see Table 3). The values of α_{\perp} also match the spectral indices derived in Sects. 4.1 and 4.2. It is satisfying to validate these values using a distinct approach in which the CIB residual is included in the data model with a power-law spectrum, rather than being subtracted by a difference. We note that the degree of anisotropy, measured by the ratios $P_{0,\perp}/P_{0,\parallel}$ in Table 6, differs by a factor of 2 between Cuts 1 and 2.

Figure 10 shows the joint posterior distributions of $\alpha_{\perp} - \alpha_{\parallel}$ and α_R , derived from the MCMC fits of Field 1 Cuts 1 and 2. The difference between the two spectral indices depends on α_R and, more generally, on the simplified model used to separate the PAH spectra from the CIB residual. In Fig. 10, the median value of $\alpha_{\perp} - \alpha_{\parallel}$ is slightly negative, but we consider the deviation from zero to be not statistically significant. We conclude that the two spectral indices are identical within a measurement error bar of 0.2 (3σ).

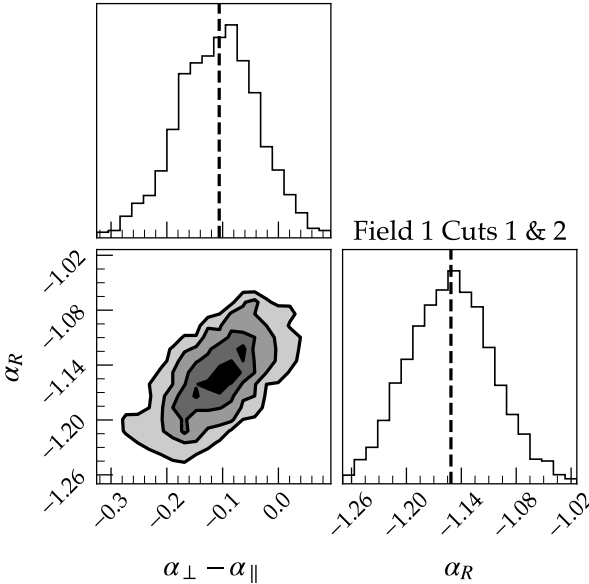


Fig. 10. Posterior distribution of $\alpha_{\perp} - \alpha_{\parallel}$ and α_R . The plot shows the joint distribution of $\alpha_{\perp} - \alpha_{\parallel}$ and α_R derived from the two power-laws fits of P_{\parallel} and P_{\perp} for Field 1 images Cuts 1 and 2 using the data model in Eq. 9.

As Lithwick & Goldreich (2001)⁷ pointed out in the context of their interpretation of radio scintillation observations, the observational effects of the parallel direction are washed out due to variations in the local orientation of anisotropy along the line of sight and across the sky. In our observations, the PAH emission is so highly anisotropic that modes perpendicular to the local orientation of anisotropy dominate the Fourier spectra in all projected orientations onto the plane of the sky. This statement entails three key facts. First, the ratios $P_{0,\perp}/P_{0,\parallel}$ in Table 6 are lower limits to the intrinsic anisotropy of the PAH emission. These limits depend on the dispersion of the local orientation of the anisotropy within the emitting medium. Second, the spectral index α_{\parallel} in Eq. 9 does not represent the spectral index of the energy cascade in the direction parallel to the magnetic field. Third, the finding that $\alpha_{\perp} - \alpha_{\parallel}$ is consistent with 0 does not exclude the possibility that the spectral indices of the turbulent energy cascade for perpendicular and parallel modes differ.

5. Relation to interstellar turbulence

In this section we present three complementary perspectives that relate the JWST Pleiades observations to interstellar turbulence. Together, they provide a framework that we hope will motivate theoretical studies aimed at interpreting the data.

5.1. Dynamical interaction between the Pleiades stars and the surrounding ISM

The Pleiades reflection nebulosity displays an impressive array of striations, which are locally nearly parallel. The origin of these striations remains a long-standing question. The idea that they could result from the dynamical interaction between the Pleiades stars with the surrounding ISM is not new. It was first discussed by Arny (1977), and remains attractive. The dust and gas observations analyzed by Herbig & Simon (2001) and

Ritchey et al. (2006) are direct evidence of a dynamical interaction. The change in dust polarization angles observed with the *Planck* data in Fig. B.2 is further evidence of this.

Projection effects make it difficult to infer the distance at which the interaction with the stars occurs. Modeling of scattered light from dust indicates that the distance between matter and the brightest Pleiades stars ranges from a few tenths to 1 parsec. Specifically, it is a few tenths of a parsec near Merope (Gibson & Nordsieck 2003b), a value that is consistent with our estimate of the radiation field intensity at the position of the Field 1 images (see Appendix C). For Merope's luminosity, a value of G in the range 10–20 corresponds to a distance from the star between 0.3 and 0.5 pc.

Gordon & Arny (1984) discuss three ways in which the gas and stars could interact: radiation pressure on the dust, stellar winds, and thermal pressure of ionized gas. Each of these could possibly account for the lack of matter near the stars. The JWST observations show that the striations extend to scales three orders of magnitude smaller than the scale of the interaction. Given that the Reynolds number of interstellar turbulence is high (Elmegreen & Scalo 2004), what we observe with the JWST is most likely the signature of a turbulent energy cascade driven by interaction, rather than the interaction itself. Energy transfer could, for example, be mediated by radiation pressure, as investigated by Callies et al. (2025).

5.2. CNM structure on the scales of the Pleiades JWST observations

The conventional framework for interpreting CNM observations (Kritsuk et al. 2018; Bellomi et al. 2020; Marchal & Miville-Deschénes 2021) is based on numerical studies of the interplay between supersonic turbulence and thermal instability (Seifried et al. 2011; Kim et al. 2013; Hennebelle & Ifrig 2014; Saury et al. 2014). The JWST data open a novel perspective by tracing the structure of the CNM on spatial scales where the turbulence turnover timescale is shorter than the CNM cooling timescale.

To support this statement, we computed the eddy turnover timescale for a power law scaling of the velocity dispersion:

$$v_{\ell} = v_L \left(\frac{\ell}{L} \right)^{\alpha_v} \quad (10)$$

$$\tau_{\text{eddy}} \equiv \ell/v_{\ell} \sim \frac{\ell^{1-\alpha_v} L^{\alpha_v}}{v_L}, \quad (11)$$

where v_{ℓ} is the dispersion of turbulent velocity on the scale ℓ and L is the scale of energy injection. We used the size of the Pleiades nebula for L , and the dispersion of velocities among gas tracers reported by Ritchey et al. (2006) as an observational estimate of v_L .

We assume that magnetic fields are dynamically important on the scale of the Pleiades nebula. We therefore used the canonical scaling of the velocity dispersion for MHD turbulence $\alpha_v = 1/4$ (Iroshnikov 1964; Kraichnan 1965). For this index, the velocity dispersion is subsonic on the scales ($\ell \lesssim 10$ mpc) statistically sampled by our JWST observations. The eddy turnover timescale is as follows:

$$\tau_{\text{eddy}} = 2 \times 10^4 \left(\frac{\ell}{10 \text{ mpc}} \right)^{3/4} \left(\frac{L}{3 \text{ pc}} \right)^{1/4} \left(\frac{v_L}{2 \text{ km s}^{-1}} \right)^{-1} \text{ yr.} \quad (12)$$

We compared τ_{eddy} with the gas cooling time, which we computed for a reference pressure in the local ISM $p/k = 4 \times 10^3 \text{ K cm}^{-3}$ using the analytical expression of the cooling

⁷ See Sect. 3 in this publication

Table 6. MCMC fit of Field 1 images with two power laws.

Image	$P_{0,\perp}$ Jy 2 sr $^{-1}$	$P_{0,\perp}/P_{0,\parallel}$	α_{\perp}	$\alpha_{\perp} - \alpha_{\parallel}$	A_R Jy 2 sr $^{-1}$	α_R
Cut 1	0.0115 ± 0.0010	92 ± 9	-3.44 ± 0.05			
Cut 2	0.0148 ± 0.0012	43 ± 4	-3.54 ± 0.04			
Cuts 1 & 2				-0.10 ± 0.07	$1.85 \pm 0.68 \cdot 10^{-6}$	-1.15 ± 0.05

Notes. Parameters of the joint fits of P_{\perp} and P_{\parallel} for Field 1 images Cuts 1 and 2, using data model in Eq. 9 with $k_0 = 10^{-2}$ pix $^{-1}$.

function in Jennings & Li (2021). For $\ell < 10$ mpc, τ_{eddy} is at least two orders of magnitude smaller than the cooling timescale of the warm neutral medium. For $\ell \sim 10$ mpc, τ_{eddy} is comparable to the cooling time of the CNM, and shorter for lower values of ℓ . It is also relevant to estimate the Field length (λ_F). Thermal instability is suppressed by conduction on scales smaller than λ_F .

$$\lambda_F = 2\pi \sqrt{\kappa T / n^2 \Lambda} \quad (13)$$

$$= 30 (\kappa / 10^5 \text{ ergs}^{-1} \text{ cm}^{-1} \text{ K}^{-1})^{0.5} \text{ mpc}. \quad (14)$$

where κ is the thermal conduction coefficient, n the gas density, T the gas temperature, and Λ the gas cooling rate (Jennings & Li 2021). The numerical value is calculated for characteristic values of n (50 cm $^{-3}$) and T (80 K) in the CNM. We find that λ_F is larger than the scales probed in our data analysis. These calculations suggest that the JWST observations of the Pleiades probe spatial scales on which turbulence in the CNM is subsonic and is no longer coupled to the thermal instability. As such, the data offer a new angle for comparing observations and theoretical models.

5.3. MHD subsonic turbulence

In order to interpret our data in the context of turbulence, one would need to connect the observational findings of this work with theoretical models of MHD turbulence scaling laws and numerical simulations (see Schekochihin 2022, for a recent review). This is obviously a difficult task and it is beyond the scope of our observational analysis to draw conclusions about specific models. Our aim is to guide future theoretical investigations. With this in mind, we present what we consider to be the four key observational results of our study.

- The mean orientation of the map striations coincides with that of the mean magnetic field projected onto the plane of the sky, as determined by the *Planck* dust polarization observations.
- The anisotropy power ratios relative to this mean orientation, 90 and 40 for Fields 1 and 2 (Table 6), are lower bounds to the local anisotropy, due to the dispersion in the orientation of the striations (Sect. 3.2). This dispersion – as determined by the widths of the angular profiles of the 2D power spectra P_{2D} – is significant (see Table 2).
- The anisotropy of P_{2D} is observed to be scale-independent within a small uncertainty set by the separation between the PAH emission and the CIB residual. We stress that for a large power anisotropy, we expect perpendicular modes to be dominant in all orientations projected onto the plane of the sky (Sect. 4.3)
- The spectral indices of the PAH power spectra measured for Field 1 match the reference value -3.5 for MHD turbulence. However, we note that the values for Field 2 differ significantly from this reference.

We discuss two possible interpretations of the origin of the power anisotropy. This choice is illustrative and not exclusive of other models. (1) Striations are formed by fast magnetosonic waves traveling perpendicularly to the mean magnetic field. (2) They are fingerprints of the anisotropy of the turbulent energy cascade of subsonic MHD turbulence. In the first case, the anisotropy is global with respect to an average guide field, while the anisotropy of the turbulence energy cascade occurs with respect to the local orientation of the magnetic field.

The first interpretation was introduced and quantified using numerical simulation in the context of molecular cloud observations by Tritsis & Tassis (2016) and Tritsis et al. (2018). It was also investigated by Beattie & Federrath (2020) using numerical simulations. More research involving dedicated simulations is required to verify whether this interpretation can reproduce the main observational results. The second is based on the Goldreich & Sridhar (1995) model of subsonic MHD turbulence. In this framework, compressible modes are sheared and passively mixed by Alfvén waves (Lithwick & Goldreich 2001). This interpretation is attractive because it links the JWST observations to the anisotropic nature of the MHD turbulence energy cascade (Boldyrev 2006; Schekochihin 2022).

6. Conclusion

We have presented and analyzed NIRCam JWST observations of the Pleiades nebula in the F335M filter centered on the PAH emission feature at 3.3 μm . These JWST observations provide an opportunity to analyze the structure of the CNM in exceptional detail, reaching spatial scales where existing observations are too limited to enable a statistical analysis. The main results of our work are summarized as follows.

We built maps of diffuse PAH emission, separating it from sources, stars, and galaxies, as well as from the extended spikes of bright stars. The stars were subtracted using an empirical template of the JWST PSF. Galaxies were identified and masked using multi-resolution image filtering to interpolate the structure of diffuse emission.

We have presented a power spectrum analysis of the diffuse emission in four images, two of which are close to the Merope star and two of which are more distant. The spectra exhibit flattening at high wavenumbers, which we identify as a CIB residual. The spectral index of this component, -1.2, is similar to that measured for galaxy clustering in CIB observations at near- and far-infrared wavelengths.

The amplitude of PAH power spectra are highly anisotropic on all scales. We characterized them in three independent ways: (1) We subtracted the CIB residual by taking the difference of the spectra computed for the JWST images near and far from Merope. (2) We differentiated anisotropic PAH emission from the isotropic CIB residual by modeling the 2D angular distribution of Fourier power. (3) We fit the power spectra in the directions parallel and perpendicular to the anisotropy orientation as

the sum of two power laws, representing the contributions from PAHs and the CIB. The three methods yield consistent results.

The PAH power spectra are measured to a spatial resolution of 0.2 mpc (40 au). They are well fitted with single power laws, with no sign of a break that could be interpreted as a signature of a characteristic scale associated with turbulence dissipation. The power-law indices are -3.5 in the two fields near Merope and -3 in the more distant areas. The magnetic field orientation inferred from dust polarization data from *Planck* is aligned with the PAH anisotropy. The power anisotropy does not change with scale.

These findings are discussed in the context of interstellar turbulence, which may be driven by the dynamical interaction between the Pleiades stars and the surrounding ISM. The observations offer a new perspective for comparing observations and theoretical models because they reveal physical scales at which CNM turbulence is decoupled from the thermal instability. Progress in interpreting the data within this framework requires follow-up theoretical work, including numerical simulations to link the PAH power spectrum to the 3D anisotropic structure of the magnetized ISM.

Acknowledgements. GV, AAC and NDR thank the STScI for DDRF Summer funding to support their research. We thank the referee for a detailed report, which helped us to clarify the discussion of the results of the data analysis in relation to interstellar turbulence. This work is based on observations made with the NASA/ESA/CSA James Webb Space Telescope which can be found in MAST: [10.17909/26am-1s4](https://doi.org/10.17909/26am-1s4). The data were obtained from the Mikulski Archive for Space Telescopes at the Space Telescope Science Institute, which is operated by the Association of Universities for Research in Astronomy, Inc., under NASA contract NAS 5-03127 for JWST. These observations are associated with program 2143.

References

Abramson, G. 2018, Research Notes of the American Astronomical Society, 2, 150

Anderson, J. 2016, Empirical Models for the WFC3/IR PSF, Instrument Science Report WFC3 2016-12, 42 pages

Anderson, J. & King, I. R. 2000, PASP, 112, 1360

Armstrong, J. W., Rickett, B. J., & Spangler, S. R. 1995, ApJ, 443, 209

Arny, T. 1977, ApJ, 217, 83

Auclair, C., Ally, E., Boulanger, F., et al. 2024, A&A, 681, A1

Beattie, J. R. & Federrath, C. 2020, MNRAS, 492, 668

Bellomi, E., Godard, B., Hennebelle, P., et al. 2020, A&A, 643, A36

Bialy, S., Zucker, C., Goodman, A., et al. 2021, ApJ, 919, L5

Boldyrev, S. 2006, Phys. Rev. Lett., 96, 115002

Bradley, L., Sipócz, B., Robitaille, T., et al. 2023, astropy/photutils: 1.8.0

Brunt, C. M., Federrath, C., & Price, D. J. 2010, MNRAS, 403, 1507

Burkhart, B. 2021, PASP, 133, 102001

Burkhart, B., Lazarian, A., Balsara, D., Meyer, C., & Cho, J. 2015, ApJ, 805, 118

Caldwell, R. R., Hirata, C., & Kamionkowski, M. 2017, ApJ, 839, 91

Callies, E., Guillet, V., Marcowith, A., Meliani, Z., & Lesaffre, P. 2025, A&A, 698, A147

Cho, J. & Lazarian, A. 2003, New A Rev., 47, 1143

Cho, J. & Vishniac, E. T. 2000, ApJ, 539, 273

Clark, S. E., Hill, J. C., Peek, J. E. G., Putman, M. E., & Babler, B. L. 2015, Phys. Rev. Lett., 115, 241302

Compiègne, M., Verstraete, L., Jones, A., et al. 2011, A&A, 525, A103

Córdoba Rosado, R., Hensley, B. S., Clark, S. E., et al. 2024, ApJ, 960, 96

Draine, B. T. & Li, A. 2007, ApJ, 657, 810

Dwek, E., Arendt, R. G., Fixsen, D. J., et al. 1997, ApJ, 475, 565

Elmegreen, B. G. & Scalo, J. 2004, ARA&A, 42, 211

Flagey, N., Boulanger, F., Verstraete, L., et al. 2006, A&A, 453, 969

Foreman-Mackey, D., Hogg, D. W., Lang, D., & Goodman, J. 2013, PASP, 125, 306

Gautier, III, T. N., Boulanger, F., Perault, M., & Puget, J. L. 1992, AJ, 103, 1313

Gibson, S. J. 2007, in Astronomical Society of the Pacific Conference Series, Vol. 365, SINS - Small Ionized and Neutral Structures in the Diffuse Interstellar Medium, ed. M. Havercorn & W. M. Goss, 59

Gibson, S. J. & Nordsieck, K. H. 2003a, ApJ, 589, 347

Gibson, S. J. & Nordsieck, K. H. 2003b, ApJ, 589, 362

Goldreich, P. & Sridhar, S. 1995, ApJ, 438, 763

Gordon, K. J. & Arny, T. T. 1984, AJ, 89, 672

Heiles, C. 1997, ApJ, 481, 193

Hennebelle, P. & Falgarone, E. 2012, A&A Rev., 20, 55

Hennebelle, P. & Ifrig, O. 2014, A&A, 570, A81

Herbig, G. H. & Simon, T. 2001, AJ, 121, 3138

Hivon, E., Górski, K. M., Netterfield, C. B., et al. 2002, ApJ, 567, 2

Hu, Y., Xu, S., Arzamasskiy, L., Stone, J. M., & Lazarian, A. 2024, MNRAS, 527, 3945

Ingalls, J. G., Miville-Deschénes, M. A., Reach, W. T., et al. 2004, ApJS, 154, 281

Iroshnikov, P. S. 1964, Soviet Ast., 7, 566

Jennings, R. M. & Li, Y. 2021, MNRAS, 505, 5238

Kandel, D., Lazarian, A., & Pogosyan, D. 2017, MNRAS, 472, L10

Kashlinsky, A., Arendt, R. G., Ashby, M. L. N., et al. 2012, ApJ, 753, 63

Kim, C.-G., Ostriker, E. C., & Kim, W.-T. 2013, ApJ, 776, 1

Knox, L. 1995, Phys. Rev. D, 52, 4307

Kraichnan, R. H. 1965, The Physics of Fluids, 8, 1385

Kritsuk, A. G., Flauger, R., & Ustyugov, S. D. 2018, Phys. Rev. Lett., 121, 021104

Lepp, S. & Dalgarno, A. 1988, ApJ, 335, 769

Lithwick, Y. & Goldreich, P. 2001, ApJ, 562, 279

Marchal, A. & Miville-Deschénes, M.-A. 2021, ApJ, 908, 186

Meisner, A. M. & Finkbeiner, D. P. 2014, ApJ, 781, 5

Melis, C., Reid, M. J., Mioduszewski, A. J., Stauffer, J. R., & Bower, G. C. 2014, Science, 345, 1029

Miville-Deschénes, M. A., Duc, P. A., Marleau, F., et al. 2016, A&A, 593, A4

Miville-Deschénes, M. A., Lagache, G., Boulanger, F., & Puget, J. L. 2007, A&A, 469, 595

Miville-Deschénes, M. A., Martin, P. G., Abergel, A., et al. 2010, A&A, 518, L104

Omont, A. 1986, A&A, 164, 159

Perrin, M. D., Sivaramakrishnan, A., Lajoie, C.-P., et al. 2014, in Society of Photo-Optical Instrumentation Engineers (SPIE) Conference Series, Vol. 9143, Space Telescopes and Instrumentation 2014: Optical, Infrared, and Millimeter Wave, ed. J. Oschmann, Jacobus M., M. Clampin, G. G. Fazio, & H. A. MacEwen, 91433X

Planck Collaboration. 2014, A&A, 571, A11

Planck Collaboration. 2016a, A&A, 596, A105

Planck Collaboration. 2016b, A&A, 596, A109

Planck Collaboration. 2016c, A&A, 586, A135

Planck Collaboration. 2020a, A&A, 641, A11

Planck Collaboration. 2020b, A&A, 641, A12

Richard, P., Ally, E., Levrier, F., Gusdorf, A., & Auclair, C. 2025, A&A, 696, A217

Rieke, M. J., Kelly, D. M., Misselt, K., et al. 2023, PASP, 135, 028001

Rigby, J. R., Lightsey, P. A., García Marín, M., et al. 2023, PASP, 135, 048002

Ritchey, A. M., Martinez, M., Pan, K., Federman, S. R., & Lambert, D. L. 2006, ApJ, 649, 788

Saury, E., Miville-Deschénes, M. A., Hennebelle, P., Audit, E., & Schmidt, W. 2014, A&A, 567, A16

Schekochihin, A. A. 2022, Journal of Plasma Physics, 88, 155880501

Seifried, D., Schmidt, W., & Niemeyer, J. C. 2011, A&A, 526, A14

Stanimirović, S. & Zweibel, E. G. 2018, ARA&A, 56, 489

Tritsis, A., Federrath, C., Schneider, N., & Tassis, K. 2018, MNRAS, 481, 5275

Tritsis, A. & Tassis, K. 2016, MNRAS, 462, 3602

Ungerechts, H. & Thaddeus, P. 1987, ApJS, 63, 645

van der Walt, S., Schönberger, J. L., Nunez-Iglesias, J., et al. 2014, PeerJ, 2, e453

Viero, M. P., Wang, L., Zemcov, M., et al. 2013, ApJ, 772, 77

Wright, E. L., Eisenhardt, P. R. M., Mainzer, A. K., et al. 2010, AJ, 140, 1868

Appendix A: Obtaining images of the diffuse emission

This appendix details and illustrates the methods used to create maps of diffuse emission out of the JWST mosaics. Figure A.1 presents a zoomed-in view of the data to illustrate the diversity of emission sources we needed to subtract or mask to obtain maps that can be used to statistically analyze the diffuse emission.

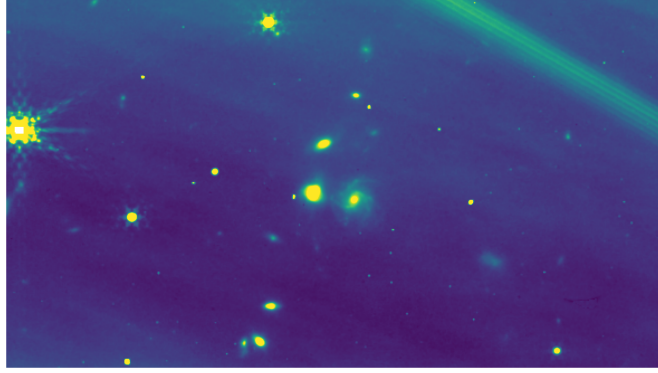


Fig. A.1. A region, about $40'' \times 20''$, of the Field 1 mosaic illustrating the diversity in emission sources in our observations: diffraction spikes, saturated stars, unsaturated stars, glitches, and galaxies of various shapes and sizes.

Appendix A.1: Removing diffraction spikes from off-field point sources

The bright star Merope in the vicinity of our field of view produces three diffraction spikes that are bright features across Field 1 (see the bottom-left panel of Fig. 1). The central one to the east of Merope aligns with the NIRCam detector arrays, and the other two are at 60° . The Merope spike with the lowest declination extends to Field 2. We modeled and removed the three spikes from Merope in Field 1, the spike from Merope that extends to Field 2, and two fainter spikes from PQ Tau in Field 1. The first three spikes are clearly visible on the bottom right panel in Fig. 1, while the fourth is barely noticeable on the bottom left panel. The last two are too faint to be visible in the figure. We illustrate our modeling with the eastern spike. To model the oblique spikes, we rotated the JWST mosaic in array coordinates by plus or minus 60 degrees to apply the same procedure.

We cut a rectangular section of the observations surrounding the diffraction spike, which is 75 to 175 pixels wide on each side (see the first panel in Fig. A.2). The width chosen depends on the intensity of the spike. In the following, columns refer to 1D cuts within the cutout image, across the spike, and rows to 1D cuts that are parallel to the spike. The steps involved in modeling and subtracting the spikes are illustrated in Fig. A.2.

The first step is to estimate the background emission around the spike. To achieve this, we masked the inner 50 to 150 pixels where the spike dominates the emission. We also masked any value above 2σ from the median in each column (using `sigma_clip` from Astropy). The data along each column are fitted with a third-order polynomial function, which we used to interpolate and fill in the diffuse emission at the position of the masked pixels. We applied a median filter to the polynomial interpolation, with a width along the spike orientation of 100 pixels, to filter out irregularities due to compact sources. The resulting map is shown in the second panel of Fig. A.2. We subtracted this background from the initial cutout image, which yielded

a map of the spike. This map still contains point and compact sources, as well as some residual diffuse emission (see the third panel in Fig. A.2).

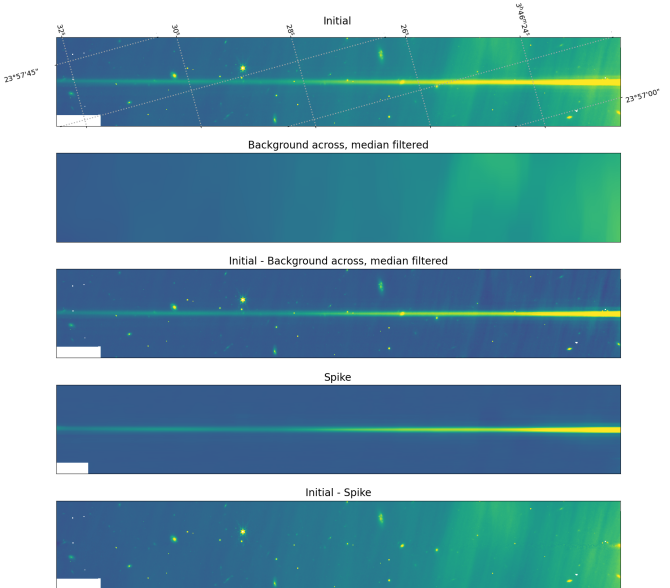


Fig. A.2. Modeling and subtraction of the spike to the east of Merope. The five panels show the same image cut out at different steps of the data cleaning (from the top): the original map; the estimation of the background with median spatial filtering; the original map with the background subtracted; the spike model; and the initial map with the spike model subtracted. A nonlinear color scaling is used to enhance the low-surface-brightness features in the field.

The second step involves modeling the spike. We estimated the gradient along the diffraction spike assuming that it can be modeled by one polynomial function that applies to each row of pixels. To obtain this polynomial function, we calculated the 2σ -clipped median of each column across the width of the spike: 150 pixels for the eastern spike of Merope, 100 pixels for the other spikes. This gave us the typical longitudinal gradient profile of the spike, which a fit with a seventh-order polynomial function (see Fig. A.3).

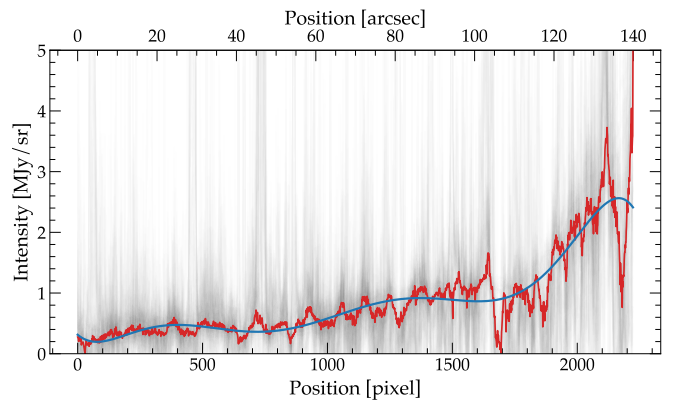


Fig. A.3. Intensity gradient along the spike to the east of Merope. In gray are all the individual longitudinal profiles within a 150-pixel-wide box around the spike, after subtraction of the diffuse background estimate and normalization across the spike (see text for details). The 2σ -clipped median profile is plotted in red, and the fit to the median using a seventh-order polynomial function is plotted in blue.

Finally, we normalized the first approximation of the spike we obtained earlier by dividing it, for each column across the spike, by the polynomial values of the longitudinal gradient. For each column, we then selected the nearest 100 columns to compute the 2σ -clipped median of this selection for each row. This gave us the profiles across the spike, assuming it does not vary on scales much shorter than 100 pixels or $6.3''$ (see Fig. A.4).

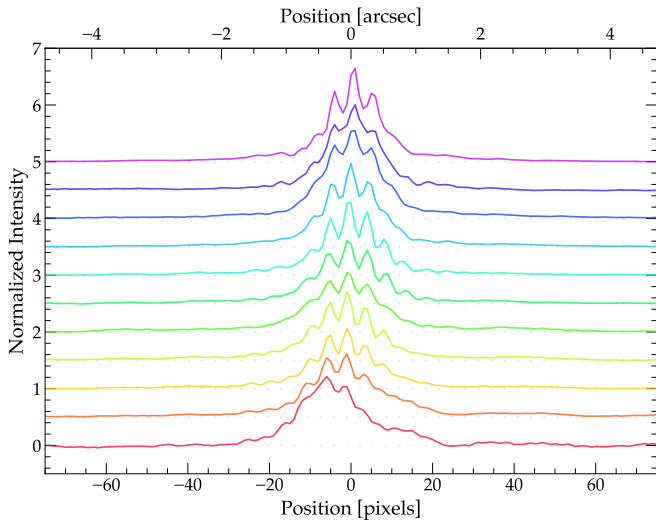


Fig. A.4. Emission profiles across the spike at multiple positions along the spike (every 200 pixels, or about $12.6''$). Each profile is offset by 0.5 with respect to the previous one. The top profile is that closest to Merope.

We note that the pattern varies smoothly along the spike. In particular, we see the peak of the profile shifts by about 2 pixels over 2000 pixels. A larger shift seems to occur at the faintest end of the spike, far from Merope, where the relative intensity of the spike is the lowest. However, even there, the shift is not greater than 7 pixels compared to the other end of the spike. Next, we rescaled the normalized profiles with the polynomial gradient to obtain the spike model shown in the fourth panel of Fig. A.2. Finally, we subtracted the model from the initial map (see the fifth panel in Fig. A.2). To assess the accuracy with which the spike is removed, we compared the residual background in the spike image, away from the central area, relative to the initial map. We find that, in the case of Merope's straight spike, the residual is typically lower than 1% at more than 75 pixels ($4.7''$) from the center of the spike (see Fig. A.5).

A limitation in our method is visible in Fig. A.6. Closer to Merope, the pattern across the spike varies on scales smaller than 100 pixels (or $6.1''$), leaving a residual trace near the edge of our observations. However, the alternative (i.e., using a smaller window than 100 pixels) would not properly filter out the sources “hidden” by the spikes. We compared these residuals with local dust emission by normalizing the profiles at the site of the spike to their median values (see Fig. A.7). In most cases, the residual of the spike is barely noticeable above the intrinsic variations of the diffuse emission, at a level of 5% of the median value of the local background. However, near Merope, the residual reaches more than 10% of that level but remains mostly random.

At this point, we thus have four mosaics, two for each field, with all large diffraction spikes removed. For each pair of mosaics, we removed the glitches by comparing the two mosaics. Each pixel whose value varies by more than 0.5 MJy/sr was replaced by the lower value in the pair.

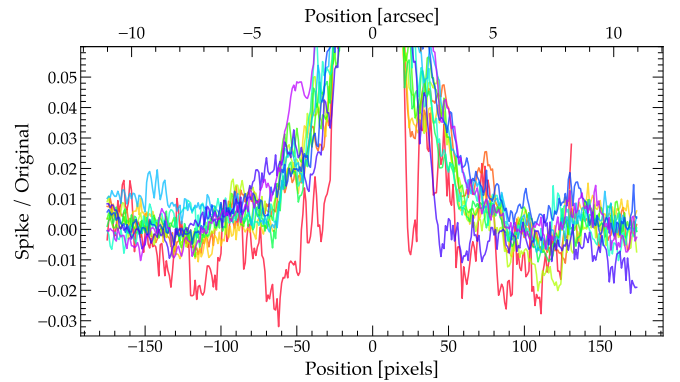


Fig. A.5. Profiles across the final spike at multiple positions along the spike (every 200 pixels, or about $12.6''$), divided by the original image. The color code is the same as in Fig. A.4.

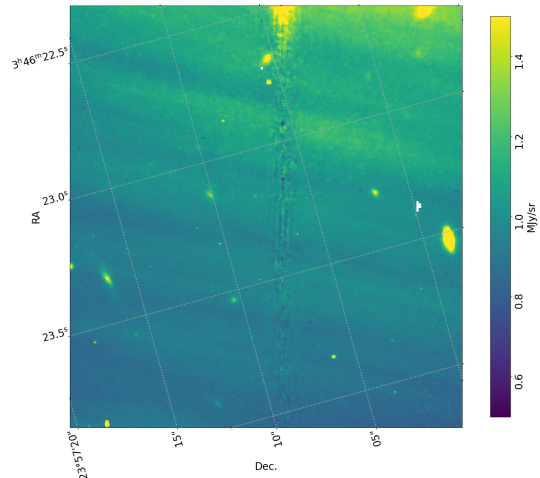


Fig. A.6. Residual of the spike to the east of Merope. The color scale has been stretched relative to other figures to enhance the faint residual.

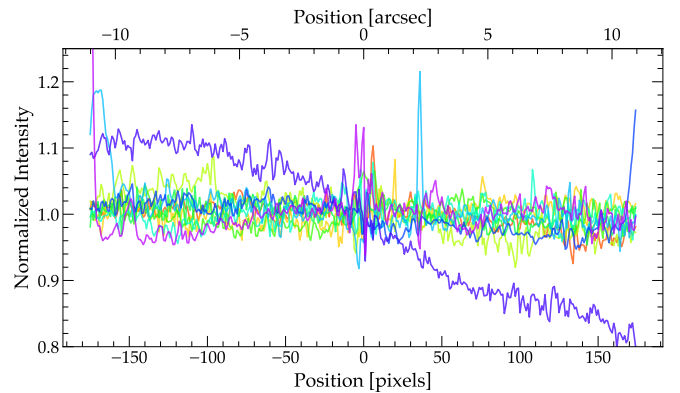


Fig. A.7. Profiles across the location of the spike at multiple positions along the spike (every 200 pixels, or about $12.6''$), obtained on the final image, normalized to equalize their median values. The color code is the same as in Fig. A.4.

Appendix A.2: Multi-scale background

Once the large spikes have been removed from the data, we modeled the diffuse emission. We used mosaics of Fields 1 and 2 from which the spikes have been removed. We computed their global median by clipping pixels above 2σ and subtracted the result from the images.

Next, we subtracted the different scales of the diffuse emission by repeating three times the following steps: (1) we computed the standard deviation of the 2σ -clipped background subtracted image, (2) we masked the bright pixels whose values are more than 15σ above the median of the entire image, (3) we performed a 2D median-filtering with a 4σ clipping without the masked pixels, and (4) we subtracted the median-filtered image. We used the `Background2D` class from `photutils` to perform these steps (Bradley et al. 2023). We applied the 2D median filter using rectangular boxes elongated along the direction of the detector arrays, which is close to the orientation of the striations. We used boxes with mean sizes of 100, 40, and 25 pixels. The ratio between the long and short sizes is 2 at all three scales. Figure A.8 illustrates the composition of the background map as smaller scales are included, as well as the residual map obtained after background subtraction for a sub-image of Field 1. There is structure in the diffuse emission at scales smaller than 25 pixels (i.e., 1.5 arcsec). This contributes noticeably, albeit minimally, to the residuals, even in Field 1, where the diffuse emission is strongest.

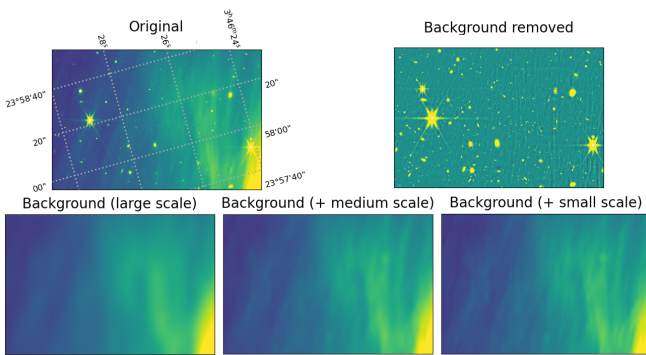


Fig. A.8. Images illustrating the multi-scale composition of the background map on a sub-image within Field 1. From the top left and going anticlockwise, the five panels show: the sub-image with the spikes removed; the background map at 100-pixel scale including the global mean; the previous map with the addition of the 40-pixel scale background; the previous map with the addition of the 25-pixel scale background; and the residual image obtained by subtracting the multi-scale background from the original image. The color scale ranges from 0.35 to 0.95 MJy/sr except for the top-right panel, where it ranges from -0.05 to 0.05 MJy/sr. A nonlinear color scaling is used to enhance the low-surface-brightness features in the field.

Appendix A.3: Removing point sources within the field

After subtracting the multi-scale background, we used the residual images to identify point sources and model the PSF. We identified point sources by recursively selecting the brightest pixel in the four combined mosaics. For each such pixel, we looked for all other neighbor bright pixels and labeled the cluster as a source before looking for the next brightest pixel in the observations. We extracted in this way the brightest 400 sources from our observations. We then visually inspected them all to separate point sources from extended sources, and ended up with 175 point sources. We did not use publicly available source extraction algorithms as they tend to identify multiple sources within each JWST PSF, as those are highly structured for the brightest sources. Our method is more robust and still functional given the small number of sources we wanted to extract.

To build an empirical PSF (ePSF), we followed the method developed by Anderson & King (2000) and Anderson (2016), which is implemented as the `EPSFBuilder` class in `photutils`, adapting it to our specific needs. In particular, we wanted to clean the spikes of the point sources more thoroughly than their cores because the spikes contaminate the diffuse emission more than the cores.

To combine the images of the selected point sources, we first centered each image to sub-pixel accuracy using the theoretical PSF of `WebbPSF` (Perrin et al. 2014) on a 301 by 301 pixel ($\sim 20''$ by $20''$). Each PSF is fitted in a squared annulus region, instead of its core, and we find that using a region of 45 by 45 pixels, with the 9 by 9 innermost pixels masked, gives the best results. The difference between the position of the brightest pixel and the computed centers of the PSFs is typically less than 0.4 pixel.

The centered PSFs are then stacked in an iterative way by our modified `EPSFBuilder` to generate the ePSF for our observations. Here, we used the same square annulus as before to align the individual PSFs with each other. The method also returns the individual best fit for each source in our collection, in their 301 by 301 original pixel grid, which we subtracted from the observations, except for the six brightest point sources that have diffraction spikes extending beyond $20''$ (see Fig. A.9). There are four point sources in Field 1 and two in Field 2, for which the core is highly saturated. If we had removed their ePSF best fit, this would have led to significant residuals across the entire 301 by 301 pixel region. For these sources, we instead waited until we added back the multi-scale background, after which we removed their diffraction spikes in the same way as for the stars off field (see Appendix A.1).

Appendix A.4: Masking the remaining sources

At this stage, we had removed all diffraction spikes from sources within and without our field of observations. We were left with masking the saturated core of bright point sources and compact sources.

To build the mask of the remaining sources, we first identified pixels that correspond to significant residuals after subtracting the ePSF fit. We computed the 2σ -clipped standard deviation for each 301 by 301 pixel image of a point source, keeping only values above a floor of 0.1 MJy/sr. Any pixel in the image whose value in the residual of the ePSF fit is greater than 10 times this standard deviation is flagged. Any pixel whose value in the ePSF fit is greater than 15 times this standard deviation is also flagged. These pixels represent fewer than 0.5% of all pixels in the four sub-mosaics and are the first included in a mask.

Next, we masked additional bright pixels. We started by creating a multi-scale background in an identical manner to what was done in the previous subsection, but now starting from a cleaner map. We then selected all pixels where the residual emission after subtraction of the multi-scale background is higher than a brightness threshold (0.035 MJy/sr for the fiducial mask). We then identified small and large clusters of masked pixels: those with fewer than or more than nine connected masked pixels. We verified that the small clusters typically correspond to faint stars or isolated glitches. Large clusters correspond either to the core of galaxies, whose shapes and sizes are very diverse (see Fig. A.1), or to the few bright point sources for which the ePSF method was not applied. Since the brightness threshold leaves the edges of bright sources unmasked, we extended the large clusters by a buffer zone of 15 additional pixels. To do this, we used the `skimage.morphology` package (van der Walt et al.

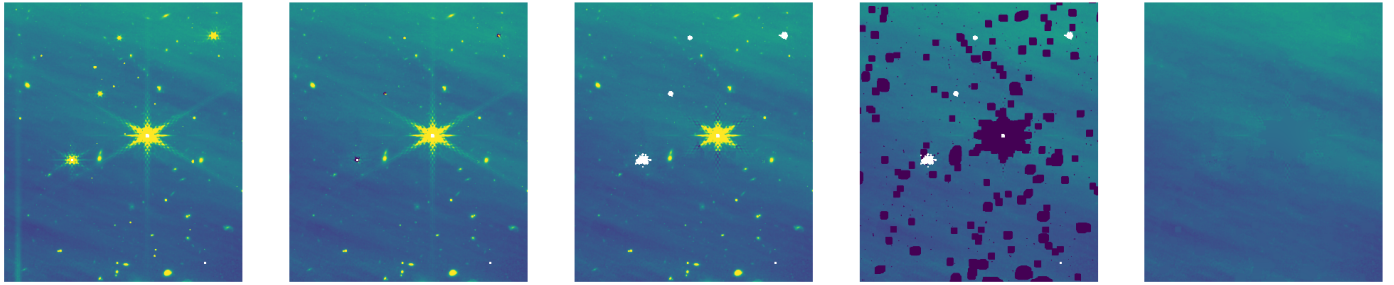


Fig. A.9. Images illustrating steps in the data cleaning on a sub-image of Field 1. From left to right: the initial image, which includes the spike of PQ Tau close to the image edge to the left; the image after the spike from PQ Tau and the in-field stars have been subtracted via the ePSF method (four stars mostly in the top half of the image); the subsequent image obtained by masking the cores of the point sources; the same region after we mask all pixels that correspond to galaxies, faint stars, and hot pixels; and the diffuse emission map.

2014). Finally, we added back the small clusters of pixels to the mask.

Starting from mosaics containing large diffraction spikes, point sources, and extended sources, we removed the spikes step by step from both the off-field and in-field sources and masked both the core of the point sources and the extended sources. This left us with mosaics containing only diffuse emission, which were used to perform the Fourier analysis presented in Sect. 3.

Appendix B: Magnetized interstellar matter near the Pleiades stars

This appendix provides a broader context for the JWST observations. *Planck* and WISE data are used to characterize the magnetized interstellar matter associated with the Pleiades nebula.

We used the dust temperature and opacity maps derived from fitting the dust spectral energy distribution at far-infrared wavelengths to a modified black body (Planck Collaboration 2016b), and the dust polarization maps at 353 GHz (Planck Collaboration 2020b). We also used the full sky image produced by Meisner & Finkbeiner (2014) from the WISE data at $12\mu\text{m}$ ⁸. The angular resolution of these maps is $5'$. However, Stokes Q and U are smoothed to $7'$ in order to improve the signal-to-noise ratio of the dust polarization.

The *Planck* and WISE maps offer complementary insights into the ISM. The dust temperature traces the localized heating of dust grains by the Pleiades stars, while the dust opacity indicates the gas column density. The conversion factor from τ_{353} to N_H for translucent molecular gas is 10^{26} H cm^{-2} (Planck Collaboration 2014). The dust polarization angles are perpendicular to the magnetic field component in the plane of the sky. The WISE image traces the emission of PAHs, the brightness of which scales linearly with the product of the intensity of the radiation field and the gas column density (Draine & Li 2007; Compiègne et al. 2011). Measurements of these observational tracers computed at the center positions of the four JWST images and for the surrounding background are listed in Table B.1. The background measurements correspond to the median value calculated for pixels within 2° of Merope where τ_{353} is smaller than 2×10^{-5} to exclude the Pleiades area.

Figure B.1 shows the *Planck* maps of dust temperature T_d and submillimeter opacity map τ_{353} at 353 GHz overlaid on the $12\mu\text{m}$ WISE image at $12''$ resolution⁹. At the distance of the

Pleiades stars, the angular size of the image corresponds to 3 pc . The dust temperature exceeds the background value across the full extent of the mid-infrared emission from the nebula. The opacity contours delineate an interstellar cloud to the south of Merope. It corresponds to a small cloud identified by Ungerechts & Thaddeus (1987) in their survey with a peak CO(1-0) brightness of 6.6 K km s^{-1} . The Merope star and the two JWST fields are located at the edge of this translucent cloud. The overlap between the contours of T_d and τ_{353} indicates that the cloud is locally heated by Merope.

Figure B.2 shows polarization angles, which have been rotated by 90° to display the magnetic field orientation in the plane of the sky. Angles were computed from the *Planck* maps after the background contribution to the Stokes Q and U maps was subtracted. Therefore, the figure illustrates the orientation of the magnetic field within the Pleiades nebula. It shows how the magnetic field changes orientation over the nebula, in particular over the cloud to the south of Merope. The black squares indicate the JWST image fields, and the red segments show the orientations of the striations (the angles θ_0 listed in Table 2). Figure B.2 shows a good match between the red and white segments. The polarization angles ψ measured at the center position of the JWST images can be found in Table 2.

Appendix C: Association with the cold neutral medium

In the paper introduction, we claim that the JWST Pleiades observations probe the structure of the CNM within a few parsecs of Merope. To support and discuss this statement, we used the *Planck* and WISE data presented in Appendix B. These data provide a global perspective on the JWST observations. The $5'$ angular resolution of the *Planck* data corresponds to a scale of 0.2 pc at the distance of Merope.

Merope lies to the front of the large (150 pc in diameter) Per-Tau bubble that was identified by Bialy et al. (2021) using 3D stellar reddening data. The star is close to the outer surface of the shell that surrounds the bubble. On smaller scales, the dust emission data presented in Appendix B show that Merope and the two JWST fields are located at the edge of a translucent cloud that has a diameter of a few parsecs. Table B.1 lists the values of the dust temperature T_d and the dust opacity τ_{353} in the center positions of the four JWST images, as well as for the surrounding background. The values of the *Planck* Stokes parameters at 353 GHz, and the PAH emission at $12\mu\text{m}$, measured on the WISE map of the entire sky produced by Meisner & Finkbeiner (2014), are also listed in the table. We used these

⁸ Image downloaded from <https://faun.rc.fas.harvard.edu/ameisner/wssa/healpix.html>

⁹ The image was downloaded from <https://irsa.ipac.caltech.edu/applications/wise>

Table B.1. *Planck* and WISE measurements.

Field	T_d K (a)	τ_{353} (b)	I MJy sr $^{-1}$ (c)	Q MJy sr $^{-1}$ (c)	U MJy sr $^{-1}$ (c)	$I_{12\mu\text{m}}$ MJy sr $^{-1}$ (d)
Field 1						
Cut 1	27.6 ± 1.2	$13.9 \pm 0.8 \cdot 10^{-6}$	0.63 ± 0.14	0.076 ± 0.025	-0.041 ± 0.025	7.3 ± 0.1
Cut 2	27.5 ± 1.2	$14.5 \pm 0.8 \cdot 10^{-6}$	0.67 ± 0.14	0.069 ± 0.025	-0.056 ± 0.025	6.1 ± 0.1
Field 2						
Cut 1	26.7 ± 0.2	$14.4 \pm 0.2 \cdot 10^{-6}$	0.66 ± 0.14	0.038 ± 0.025	-0.105 ± 0.025	3.3 ± 0.1
Cut 2	25.5 ± 0.2	$13.8 \pm 0.2 \cdot 10^{-6}$	1.07 ± 0.14	0.035 ± 0.025	-0.122 ± 0.025	2.4 ± 0.1
Background^e	18.6 ± 0.5	$12.3 \pm 3 \cdot 10^{-6}$	0.58 ± 0.14	0.055 ± 0.025	0.016 ± 0.025	0.34 ± 0.10

Notes. (a) Dust temperature from *Planck* data at 5' resolution. (b) Dust opacity at 353 GHz from *Planck* data at 5' resolution. (c) Stokes I , Q and U at 353 GHz measured at the center of the JWST images on *Planck* maps smoothed to a 7' beam. The values for Fields 1 and 2 are background subtracted. (d) Brightness at 12 μm measured at the center of the JWST images on the WISE all-sky map (Meisner & Finkbeiner 2014). The values for Fields 1 and 2 are background subtracted. (e) Median values over the background area. The error bars are the standard deviation of pixel values. Uncertainties on the median values are one order of magnitude smaller.

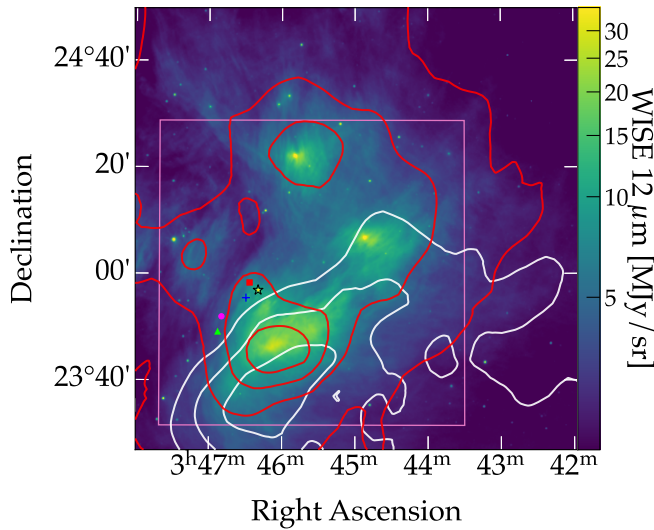


Fig. B.1. Dust temperature and opacity maps overlaid on the 12 μm WISE image at full angular resolution. The dust opacity at 353 GHz and the dust temperature, as derived from the analysis of *Planck* data, are shown with white contours for $\tau_{353} = 2, 3$, and 4×10^{-5} and in red contours for $T_d = 20, 23, 26$, and 29 K. Merope is marked with a star, the centers of the JWST images with a red square, Field 1 Cuts 1 and 2 with a blue plus sign, and Field 2 Cuts 1 and 2 with a purple circle and a green triangle. The pink box displays the location of the image of dust polarization angles presented in Fig. B.2.

data to estimate the radiation field intensity and gas column density at the location of the JWST fields.

The radiation field intensity can be estimated from the dust temperature using the formula

$$G = (T_d/T_{\text{BG}})^{(4+\beta)}, \quad (\text{C.1})$$

with a spectral index $\beta = 1.6$ (Planck Collaboration 2014). The factor G measures the radiation field intensity normalized to its value within the background ISM, away from the Pleiades stars. This formula yields G values ranging from 6 to 9 at the position of the JWST fields. The opacity values listed in Table B.1 include the Galactic background. To estimate the column density of the cloud associated with Merope, we needed to subtract this contribution. This subtraction introduces a large uncertainty equal to the dispersion of opacity values measured over the background area, which is listed as the error bar in the background line of the

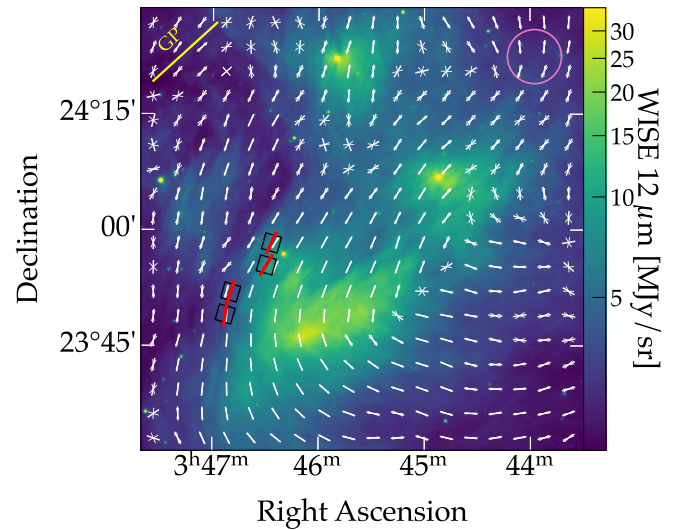


Fig. B.2. *Planck* dust polarization angles rotated by 90° to display the magnetic field orientation on the plane of the sky. The white segments indicating the dust polarization angle are plotted alongside thinner adjacent segments that represent 1 σ error bars. The background image is the same 12 μm WISE image at full resolution as in Fig. B.1. The circle in the top-right corner shows the beam of the *Planck* data at half maximum. The black squares indicate the JWST image fields, with the red segments showing the orientations of the striations in the JWST maps. The yellow line in the top-left corner shows the orientation of the Galactic longitude axis.

table. Taking into account this uncertainty, we assumed that the column density of the cloud at the positions of the JWST fields cannot be much larger than $5 \times 10^{20} \text{ H cm}^{-2}$.

The 12 μm brightness allows us to crosscheck the estimates of G and N_H . In the solar neighborhood, the mean emission at 12 μm is 0.3 MJy sr $^{-1}$ for a column density N_H of $10^{21} \text{ H cm}^{-2}$ (Compiègne et al. 2011). For fixed PAH abundance and emission properties, this emission scales linearly with the product $G \times N_H$ (Draine & Li 2007; Compiègne et al. 2011). Based on the 12 μm brightness values in Table B.1, we estimated the product $G \times N_H$ to be 16 and 7 for Fields 1 and 2, where N_H is expressed in units of $10^{21} \text{ H cm}^{-2}$. These values suggest that the estimates of G and N_H derived from dust temperature and opacity are somewhat underestimated. This could be due to beam smoothing and the superposition of cloud and background emissions, which were not

considered when fitting the dust temperature and opacity. In any case, the estimates of G and N_H support our assertion that the JWST observations characterize emission from CNM within a few parsecs of Merope. The value of G is 10 at a distance of 0.5 pc from Merope. The contribution to N_H of warm gas with densities of a few tenths of a H cm^{-3} across this distance is negligible.

We also estimated the contribution of the Galactic background to the JWST power spectra. To achieve this, we used the scaling law established by [Miville-Deschénes et al. \(2007\)](#) when analyzing Infrared Astronomical satellite (IRAS) data. The fraction of power contributed by the Galactic background f^{BG} is estimated using the following formula:

$$f^{\text{BG}} = (I_{3.5}^{\text{BG}}/I_{3.5})^2, \quad (\text{C.2})$$

where $I_{3.5}$, the brightness in the center of a JWST image in the F335M filter, is obtained by multiplying the values I_{12} and $I_{3.5}/I_{12}$ in Table 1. To obtain the background brightness $I_{3.5}^{\text{BG}}$ in the F335M filter, we scaled the background brightness at $12\mu\text{m}$ listed in Table B.1 by the intensity ratio $6\ 10^{-2}$, as determined in the study of [Flagey et al. \(2006\)](#). We obtain values of f^{BG} $\sim 0.1\%$ for the Field 1 images and between one and a few percent for the Field 2 images. These low values support the link that the paper makes between the JWST power spectra and the CNM near the Pleiades stars.